

ESD ACCESSION LIST

XRRRI Call No. 83008

Copy No. 1 of 2 cys.

2

Solid State Research

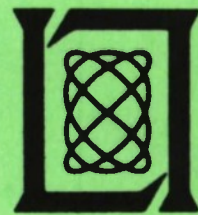
1975

Prepared for the Department of the Air Force
under Electronic Systems Division Contract F19628-73-C-0002 by

Lincoln Laboratory

MASSACHUSETTS INSTITUTE OF TECHNOLOGY

LEXINGTON, MASSACHUSETTS



Approved for public release; distribution unlimited.

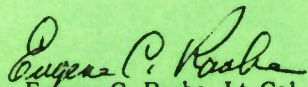
ADA 013163

The work reported in this document was performed at Lincoln Laboratory, a center for research operated by Massachusetts Institute of Technology, with the support of the Department of the Air Force under Contract F19628-73-C-0002.

This report may be reproduced to satisfy needs of U.S. Government agencies.

This technical report has been reviewed and is approved for publication.

FOR THE COMMANDER



Eugene C. Raabe, Lt. Col., USAF
Chief, ESD Lincoln Laboratory Project Office

Non-Lincoln Recipients

PLEASE DO NOT RETURN

Permission is given to destroy this document
when it is no longer needed.

MASSACHUSETTS INSTITUTE OF TECHNOLOGY
LINCOLN LABORATORY

SOLID STATE RESEARCH

QUARTERLY TECHNICAL SUMMARY REPORT
TO THE
AIR FORCE SYSTEMS COMMAND

1 FEBRUARY - 30 APRIL 1975

ISSUED 26 JUNE 1975

Approved for public release; distribution unlimited.

LEXINGTON

MASSACHUSETTS

ABSTRACT

This report covers in detail the solid state research work of the Solid State Division at Lincoln Laboratory for the period 1 February through 30 April 1975. The topics covered are Solid State Device Research, Quantum Electronics, Materials Research, and Microelectronics. The Microsound work is sponsored by ABMDA and is reported under that program.

CONTENTS

Abstract	iii
Introduction	v
Reports on Solid State Research	viii
Organization	xii
I. SOLID STATE DEVICE RESEARCH	1
A. Integrated GaAs-AlGaAs Double-Heterostructure Lasers	1
B. Selenium Ion-Implanted GaAs	4
C. Gain Profile in External Cavity Controlled GaAs Lasers	6
D. PbS MIS Devices for Charge-Coupled Infrared Imaging	11
II. QUANTUM ELECTRONICS	17
A. Optically Pumped Semiconductor Lasers	17
1. Long-Path Monitoring Techniques and Atmospheric Spectroscopy with InSb Laser	17
2. CW InAs Lasers Optically Pumped with GaAs Diode Lasers	19
3. Diode-Pumped Pulsed Semiconductor Lasers	21
B. Infrared Nonlinear Materials	23
1. Infrared Transmission of Li-Diffused CdGeAs ₂ Samples	23
2. SHG Efficiency in CdGeAs ₂ at Liquid Nitrogen Temperature	23
3. Surface Damage Threshold for CdGeAs ₂ , AgGaSe ₂ , AgGaS ₂ , Ti ₃ AsSe ₃ , and Ge	25
C. Electro-optic Modulator for Submillimeter Radiation	30
III. MATERIALS RESEARCH	33
A. Crystallization of Amorphous Silicon Films by Nd:YAG Laser Heating	33
B. Measurement of Ionic Conductivity in Solid Electrolytes	37
C. Surface Loss Functions of Titanium and Vanadium Oxides Derived from Optical Data	39
D. Electron Microprobe Analysis of Ga _{1-x} Al _x As Layers	42
IV. MICROELECTRONICS	45
A. Charge-Coupled Imaging Arrays	45
B. Tapped Delay Line	47
C. Silicon Schottky-Diode Arrays for Coherent Integration of Acoustic Signals	51
D. Gallium Arsenide Vapor Epitaxy	52

INTRODUCTION

I. SOLID STATE DEVICE RESEARCH

An integrated GaAs-AlGaAs double-heterostructure laser emitting at approximately 9100 \AA into a high-purity GaAs passive waveguide has been fabricated and characterized. The lowest measured room-temperature threshold current density for the lasers was 7.5 kA/cm^2 , and the measured external differential quantum efficiencies of the laser-waveguide combination were about 3.5 percent.

Electrically active donor impurity concentrations above 10^{18} cm^{-3} have been achieved in GaAs by Se-ion implantation. By using pyrolytic Si_3N_4 encapsulation and a post-implantation annealing temperature of 900°C , a peak electron carrier concentration of $3.5 \times 10^{18} \text{ cm}^{-3}$ was measured for a sample implanted with $1 \times 10^{14} \text{ Se ions/cm}^2$.

The gain profile of external cavity controlled GaAs single (SH)- and double (DH)-heterostructure lasers was measured for various active region dopants and under different device operating conditions. For SH devices, the gain profile was found to be comprised of two regions: a lower energy abnormal region which is characterized by a time delay that increases with increasing current, and a higher energy portion with normal time-delay behavior. For DH devices, only the normal delay was observed.

An experimental investigation of PbS metal-insulator-semiconductor (MIS) devices has led to results which suggest the feasibility of developing a monolithic two-dimensional charge-coupled imaging device in a narrow-gap semiconductor which would be operable at 77 K and have moderate sensitivity out to about $3.5 \text{ }\mu\text{m}$. A storage time of $\sim 2.3 \text{ sec}$ was measured, which is nearly two orders of magnitude longer than the $1/30\text{-sec}$ frame time for standard two-dimensional imaging.

II. QUANTUM ELECTRONICS

The GaAs-pumped CW InSb laser has been used to carry out atmospheric spectroscopy of H_2O , NO , and C_2H_4 over a 7-m path. Continuous operation in InAs and pulsed operation in GaSb and $\text{PbS}_{1-x}\text{Se}_x$ ($x = 0, 0.2, 0.4$) also have been obtained with GaAs diode laser pumping. Spectra of NH_3 in the $3\text{-}\mu\text{m}$ region were taken with the InAs laser.

Work is continuing on the evaluation of nonlinear optical materials for the middle infrared. The effects on optical attenuation of annealing CdGeAs_2 in a lithium atmosphere have been examined, and a study of the source of the short-wavelength infrared attenuation has been undertaken. Second-harmonic generation in this material exhibits saturation effects at liquid nitrogen temperature, with a 12.8-percent external conversion efficiency for a 12.1-mm-long crystal. Optical surface damage measurements have been made at $10.6 \text{ }\mu\text{m}$ for CdGeAs_2 , AgGaSe_2 , AgGaS_2 , Tl_3AsSe_3 , and Ge.

An electro-optic modulator for submillimeter radiation in LiTaO_3 has been developed. The index and electro-optic coefficient are enhanced by lattice contributions in this wavelength region. A 4-cm-long crystal, with a 10-kV applied field at 600 Hz, gave greater than 90-percent modulation of HCN laser radiation. Modulation up to 250 kHz was also observed, limited only by the modulation drive.

III. MATERIALS RESEARCH

Amorphous Si films deposited by RF sputtering have been converted into crystalline Si by heating with focused Nd:YAG laser radiation. Laser crystallization is potentially a technique for preparing large-grain Si films at a cost low enough to permit their use in solar cells for large-scale terrestrial applications.

The ionic conductivity of solid electrolytes has been investigated by measuring the transient current response of such materials to trains of constant-voltage pulses. Measurements of this type have shown that ion diffusion plays a significant role in the conductivity of polycrystalline materials exhibiting fast Na^+ -ion transport, which are being studied for possible use as ceramic membranes in the Na-S secondary battery.

In connection with a study of the role played by surface states in the catalytic behavior of TiO_2 anodes in the photoelectrolysis of water, the surface loss functions of titanium and vanadium oxides have been calculated from the bulk dielectric functions determined from optical data. The results are in good agreement with those obtained by electron energy-loss spectroscopy, and confirm the presence of a strong peak attributed to electron transitions between $3d^1$ states of the Ti^{3+} ion.

An electron microprobe procedure has been developed for quantitative analysis of Ga and Al in thin layers (1 to 5 μm) of $\text{Ga}_{1-x}\text{Al}_x\text{As}$ grown on GaAs substrates by liquid-phase epitaxy. The standard used for determining both elements is a $\text{Ga}_{1-x}\text{Al}_x\text{As}$ layer 23 μm thick whose homogeneity has been checked by microprobe measurements.

IV. MICROELECTRONICS

Bulk lifetimes in the starting materials for the fabrication of the 100×1 linear CCD imaging arrays and the 30×30 two-dimensional CCD imaging arrays used as prototypes for the TDAR program have been found to be low, leading to unacceptably high values of dark current (greater than 500 nA/cm^2) in the final devices. Adding 5% HCl during oxidation in dry O_2 has raised the bulk lifetime to as high as 2.3 msec in otherwise unprocessed wafers. Experiments are under way to determine if subsequent CCD processing can proceed without causing lowered lifetimes and the resulting high dark current.

A surface acoustic wave tapped delay line consisting of two lithium niobate crystals mounted in a single package has been delivered to the R. F. Systems Group for evaluation. The complete line has 11 taps, a maximum delay of 66 μsec , and a 3-dB bandwidth of 100 MHz. The output transducers have been raised in design center frequency from the nominal 300 MHz to compensate for the frequency dependence of

propagation loss. Work on experimental short delay lines has shown that the mid-band dip in output transducer response can be reduced from 3.5 to 1.4 dB by tuning the input transducer with a series inductor and increasing the number of fingers in the output transducer from 5 to 6.

A silicon Schottky barrier diode array and a lithium niobate surface acoustic wave delay line mounted in close proximity to one another form a memory and correlator structure. In order to allow repetitive write-ins of the same signal waveform, the 5- μm platinum Schottky contacts are overlaid with 10- μm \times 10- μm \times 1200- \AA -thick pads of high-resistivity polycrystalline silicon which have a high capacity toward the bulk silicon and allow sequential voltage pulses to add charge to the diodes without erasing the charge already stored. A coherent integration gain of 20 dB over what is achieved with a single write-in pulse has been shown.

A GaAs vapor epitaxy system has been designed and built to grow multiple layers with different doping levels on highly doped substrates for microwave and integrated optical devices. The system uses the $\text{AsCl}_3\text{-Ga-H}_2$ method in conjunction with a vertical furnace. Undoped layers have been grown with LN_2 mobilities of up to 80,000 $\text{cm}^2/\text{V sec}$. Sulfur doping has been used to produce layers with carrier concentration from 5×10^{14} to $3 \times 10^{18} \text{ cm}^{-3}$.

REPORTS ON SOLID STATE RESEARCH

15 February through 15 May 1975

PUBLISHED REPORTS

Journal Articles

JA No.

4373	Thickness and Surface Morphology of GaAs LPE Layers Grown by Supercooling, Step-Cooling, Equilibrium-Cooling, and Two-Phase Solution Techniques	J. J. Hsieh	J. Cryst. Growth <u>27</u> , 49 (1974), DDC AD-A008298
4389	The Influence of 3d Transition Metal Substitution on the Magnetic Properties of MnGaGe	J. B. Goodenough G. B. Street* K. Lee* J. C. Suits*	J. Phys. Chem. Solids <u>36</u> , 451 (1975)
4402	p-n Junction PbS _{1-x} Se _x Photodiodes Fabricated by Se ⁺ Ion Implantation	J. P. Donnelly T. C. Harman	Solid-State Electron. <u>18</u> , 288 (1975)
4415	On the Wigner Distribution Function for an Oscillator	R. W. Davies K. T. R. Davies*	Ann. Phys. <u>89</u> , 261 (1975)
4432	Auger Spectroscopy Studies of the Oxidation of Amorphous and Crystalline Germanium	V. E. Henrich J. C. C. Fan	J. Appl. Phys. <u>46</u> , 1206 (1975)
4442	Optically Pumped Vibrational Transition Laser in OCS	H. R. Schlossberg* H. R. Fetterman	Appl. Phys. Lett. <u>26</u> , 316 (1975)
4454	Optically Pumped cw InSb Lasers for NO Spectroscopy	A. S. Pine N. Menyuk	Appl. Phys. Lett. <u>26</u> , 231 (1975)
4456	Light Scattering Lineshape in Opaque Materials	G. Dresselhaus A. S. Pine	Solid State Commun. <u>16</u> , 1001 (1975)

Meeting Speeches

MS No.

3778	Oxide Engineering	J. B. Goodenough	J. Solid State Chemistry <u>12</u> , 148 (1975), DDC AD-A008308
3822	Surface Acoustoelectric Correlator with Surface State Memory	J. H. Cafarella A. Bers* E. Stern	1974 IEEE Ultrasonics Symposium Proceedings, Milwaukee, 11-13 November 1974, pp. 216-219

* Author not at Lincoln Laboratory.

MS No.

3830	Tunable Infrared Lasers	K. W. Nill	Optical Engineering 13 , 516 (1974), DDC AD-A008296
3883	On the Performance and Limitations of the Surface- Wave Resonator Using Grooved Reflectors	R. C. M. Li R. C. Williamson D. C. Flanders* J. A. Alusow	1974 IEEE Ultrasonics Symposium Proceedings, Milwaukee, 11-13 November 1974, pp. 257-262
3890	Surface Wave Correlator – Convolver with Memory	A. Bers* J. H. Cafarella	1974 IEEE Ultrasonics Symposium Proceedings, Milwaukee, 11-13 November 1974, pp. 778-787
3891	Problems Encountered in High-Frequency Surface- Wave Devices	R. C. Williamson	1974 IEEE Ultrasonics Symposium Proceedings, Milwaukee, 11-13 November 1974, pp. 321-328
3894	16-Channel Surface-Acoustic- Wave Filter Bank	V. Dolat J. Melngailis	1974 IEEE Ultrasonics Symposium Proceedings, Milwaukee, 11-13 November 1974, pp. 756-759

* * * * *

UNPUBLISHED REPORTS

Journal ArticlesJA No.

4393	Unified Model of the Insulator- Metal Transition in Ti_2O_3 and the High-Temperature Tran- sition in V_2O_3	H. J. Zeiger	Accepted by Phys. Rev. B
4473	Low-Threshold, cw $LiNdP_4O_{12}$ Laser	S. R. Chinn H. Y-P. Hong	Accepted by Appl. Phys. Lett.
4476	Efficient InSb Laser with Resonant Longitudinal Optical Pumping	N. Menyuk A. S. Pine A. Mooradian	Accepted by IEEE J. Quantum Electron.
4481	Observation of a Very Narrow Surface Resonance on Single- Crystal Aluminum	V. E. Henrich	Accepted by Surf. Sci.
4498	PbS MIS Devices for Charge- Coupled Infrared Imaging Applications	F. J. Leonberger A. L. McWhorter T. C. Harman	Accepted by Appl. Phys. Lett.
4502	Crystal Structure of $NdLiP_4O_{12}$	H. Y-P. Hong	Accepted by Mater. Res. Bull.

* Author not at Lincoln Laboratory.

JA No.

4506	Silicon and Selenium Ion Implanted GaAs Reproducibly Annealed at Temperatures up to 950°C	J. P. Donnelly W. T. Lindley C. E. Hurwitz	Accepted by Appl. Phys. Lett.
4508	Electrical Characterization of Epitaxial Layers	G. E. Stillman C. M. Wolfe	Accepted by Thin Solid Films
4509	As ⁺ -Ion Implanted PbTe p-n Junction Photodiodes	J. P. Donnelly T. C. Harman	Accepted by Solid-State Electron.

Meeting Speeches*

MS No.

3337R	Lasers for Photochemical Applications	A. Mooradian	M.I.T. Industrial Liaison Seminar, East Brunswick, New Jersey, 24 March 1975
3812A	Nonlinear Materials: Present and Future Device Applications	A. Mooradian	M.I.T. Industrial Liaison Seminar, M.I.T., 8 April 1975
3971	Concentrated-Rare-Earth Laser Materials	S. R. Chinn J. W. Pierce H. Y-P. Hong	
3827A	Spin-Flip Raman Scattering	S. R. J. Brueck	
3935	Partially Filled Atomic Cores in Fluorides	J. B. Goodenough	American Chemical Society, Philadelphia, 10 April 1975
3936	Preparation of Sn-Doped In ₂ O ₃ Films by RF Sputtering	F. J. Bachner J. C. C. Fan	147th Meeting, Electrochemical Society, Toronto, Canada, 11-16 May 1975
3937	Preparation and Application of Transparent Heat Mirrors for Solar-Energy Collection	J. C. C. Fan F. J. Bachner	77th Annual Meeting and Exposition, Electronics Division, American Ceramic Society, Washington, D.C., 3-8 May 1975
3949	Tunable-Laser Measurements of Atmospheric Infrared Absorption Parameters	R. S. Eng K. W. Nill	Topical Meeting, Applications of Laser Spectroscopy, Anaheim, California, 19-21 March 1975
3950	Solar-Energy Collection-Conversion	J. B. Goodenough	Seminar, Arizona State University, Tempe, 14 February 1975

* Titles of Meeting Speeches are listed for information only. No copies are available for distribution.

<u>MS No.</u>			
3963	Narrow-Gap-Semiconductor Tunable Diode Lasers	K. W. Nill	} American Physical Society Meeting, Denver, 31 March - 3 April 1975
4015	Multiphonon Absorption in Laser Windows	T. F. Deutsch	
3972	Structure and Properties of Magnetic Materials	J. B. Goodenough	American Crystallographic Association Symposium, Charlottesville, Virginia, 9-13 March 1975
3985	Planar InSb Photodiodes Fabricated by Be and Mg Ion Implantation	C. E. Hurwitz J. P. Donnelly	} IRIS Detector Specialty Group Meeting, Ft. Monmouth, New Jersey, 11-13 March 1975
3986	Planar HgCdTe Quadrantal Heterodyne Arrays with GHz Response at 10.6 μm	D. L. Spears	
3987	High Sensitivity Wide Bandwidth HgCdTe Photodiodes for Heterodyne Detection in the 5 to 12 μm Region	D. L. Spears I. Melngailis T. C. Harman	
3987A	High Sensitivity Wide Bandwidth HgCdTe Photodiodes for Heterodyne Detection in the 5 to 12 μm Region	D. L. Spears	Seminar, Honeywell Radiation Center, Lexington, Massachusetts, 8 April 1975
3987B	GHz Bandwidth HgCdTe Photodiodes for Heterodyne Detection in the 4 to 12 μm Region	D. L. Spears	Seminar, Electrical Engineering and Optics, M.I.T., 17 April 1975
4052	Electrical Properties of Cadmium Sulfide	A. J. Strauss	NSF Workshop on CdS Cells, University of Delaware, Newark, 1 May 1975

ORGANIZATION

SOLID STATE DIVISION

A. L. McWhorter, *Head*
I. Melngailis, *Associate Head*
C. R. Grant, *Assistant*
P. E. Tannenwald
H. J. Zeiger

QUANTUM ELECTRONICS

A. Mooradian, *Leader*
P. L. Kelley, *Associate Leader*

Barch, W. E.	Heckscher, H.
Breck, S. R. J.	Kildal, H.
Burke, J. W.	Larsen, D. M.
Chinn, S. R.	Mandel, P.*
DeFeo, W. E.	Menyuk, N.
Dentsch, T. F.	Monlton, P. F.*
Eng, R. S.	Parker, C. D.
Fetterman, H. R.	Pine, A. S.
Hancock, R. C.	

APPLIED PHYSICS

A. G. Foyt, *Leader*
T. C. Harman, *Assistant Leader*
C. E. Hurwitz, *Assistant Leader*

Belanger, L. J.	McBride, W. F.
Calawa, A. R.	Orphanos, W. G.
Carter, F. B.	Paladino, A. E.
DeMeo, N.	Reeder, R. E.
Donnelly, J. P.	Rossi, J. A.
Ferrante, G. A.	Spears, D. L.
Groves, S. H.	Stillman, G. E.
Krohn, L., Jr.	Walpole, J. N.
Leonberger, F. J.	

ELECTRONIC MATERIALS

J. B. Goodenough, *Leader*
A. J. Strauss, *Associate Leader*

Anderson, C. H., Jr.	Kolesar, D. F.
Animalu, A. O. E.	LaFleur, W. J.
Button, M. J.	Mastromattei, F. L.
Delaney, F. J.	Mayroides, J. G.
Dresselhaus, G.	Mroczkowski, J. H.
Dwight, K., Jr.	Oli, B.*
Fahy, R. E.	Owens, E. B.
Fan, J. C. C.	Palm, B. J.
Feldman, B.	Pantano, J. A.
Finn, M. C.	Pierce, J. W.
Henrich, A. E.	Plonko, M. C.
Hong, H. Y-P.	Reed, T. B.
Hsieh, J. J.	Tcherney, D. I.
Iseler, G. W.	Tracy, D. M.
Kafalas, J. A.	Zavacky, P. M.

MICROSOFT

E. Stern, *Leader*
R. C. Williamson, *Assistant Leader*

Alnsow, J. A.	Kernan, W. C.
Brogan, W. T.	Li, R. C. M.
Cafarella, J. H.	Melngailis, J.
Dolat, A. S.	Ralston, R. W.
Efremow, N., Jr.	Smith, H. I.
Ingebrigtsen, K.	

MICROELECTRONICS

W. T. Lindley, *Leader*
F. J. Bachner, *Assistant Leader*

Beatrice, P. A.	Gray, R. A.
Bozler, C. O.	Lincoln, G. A., Jr.
Burke, B. E.	McGonagle, W. H.
Clough, T. F.	Mountain, R. W.
Cohen, R. A.	Murphy, R. A.
Durant, G. L.	Pichler, H. B.
Foley, G. H.	Smythe, D. L.
Grant, L. L.	Wilde, R. E.

* Research assistant

I. SOLID STATE DEVICE RESEARCH

A. INTEGRATED GaAs-AlGaAs DOUBLE-HETEROSTRUCTURE LASERS

The capability of integrating a laser source with a passive optical waveguide is an important element in the fabrication of a monolithic integrated optical circuit. One such structure, which utilizes the "twin guide" concept whereby light from a GaAs-AlGaAs laser is coupled downward into an AlGaAs waveguide parallel to the laser active region, has been demonstrated by Suematsu *et al.*¹ Reinhart and Logan² also have described a different structure wherein a passive AlGaAs waveguide layer has been included within the Fabry-Perot cavity of a GaAs-AlGaAs laser.

Another approach, which we have successfully implemented, involves the integration of an independent Fabry-Perot GaAs-AlGaAs double-heterostructure laser with a high-purity GaAs passive waveguide. This structure has the features that it is planar, the fabrication and operation of the laser are completely independent of the waveguide, and it is compatible with Fabry-Perot, distributed feedback (DFB),³ or distributed Bragg reflector (DBR)⁴ lasers. Furthermore, it utilizes the low-loss ($\alpha \leq 1 \text{ cm}^{-1}$ at $\lambda = 9100 \text{ \AA}$), high-purity waveguides⁵ in which integrated electroabsorption modulators⁵⁻⁷ and both electroabsorption⁸ and InGaAs avalanche detectors⁹ have been demonstrated.

A schematic cross section of the laser-waveguide structure is shown in Fig. 1-1. Fabrication of the devices begins with a typical GaAs-AlGaAs double-heterostructure wafer grown by liquid-phase epitaxy on a (100)-oriented substrate. The active region was doped heavily p-type with silicon in order to achieve laser emission near 9100 \AA for low loss in the GaAs waveguide. Using photolithographically defined pyrolytic SiO_2 as a mask, we created rectangular mesas 300 \mu m long, 45 or 90 \mu m wide, and 10 to 12 \mu m high by chemically etching ($1\text{H}_2\text{SO}_4 : 8\text{H}_2\text{O}_2 : 1\text{H}_2\text{O}$ at 2°C) down through the grown layers to the substrate. Orientation of

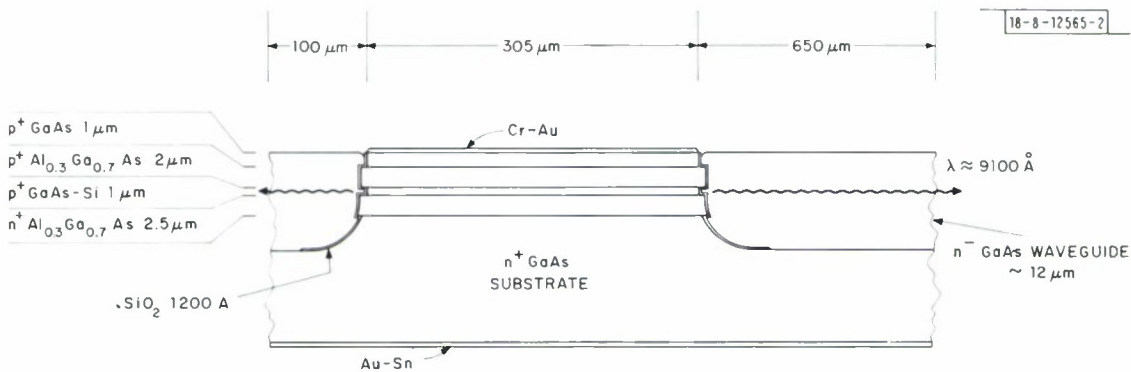


Fig. 1-1. Artist's representation of cross section of GaAs-AlGaAs double-heterostructure laser integrated into high-purity GaAs waveguide. Dimensions shown are typical. Laser widths were typically 45 and 90 \mu m .

the rectangles along (100) directions resulted in mesas with walls perpendicular to the (100) wafer surface,¹⁰ the parallel end faces of the mesa then forming the end mirrors for the Fabry-Perot cavity. Etched and grown mesa Fabry-Perot homojunction lasers have been described earlier by Dobkin *et al.*¹¹ and by Blum *et al.*,¹² respectively. After etching of the mesas, the superoxol etch described by Logan and Reinhart¹³ was used to selectively remove about 1 μm of GaAs without etching the AlGaAs. This secondary etch appeared to improve the parallelism of end faces which had not etched exactly perpendicular to the wafer surface during the formation of the mesas. However, the necessity or even the beneficial effect of this etch has not been established at present. In order to provide a reflecting dielectric mismatch between the end faces of the Fabry-Perot laser and the high-purity GaAs waveguide to be grown around the mesas, a layer of pyrolytic SiO_2 , 1200 to 1500 \AA thick, was deposited, photolithographically defined, and etched leaving only the walls and tops of the mesas covered.[†] By vapor-phase epitaxy, the high-purity GaAs waveguide material then was grown on the substrate surrounding the mesas to a thickness approximately equal to the mesa height.

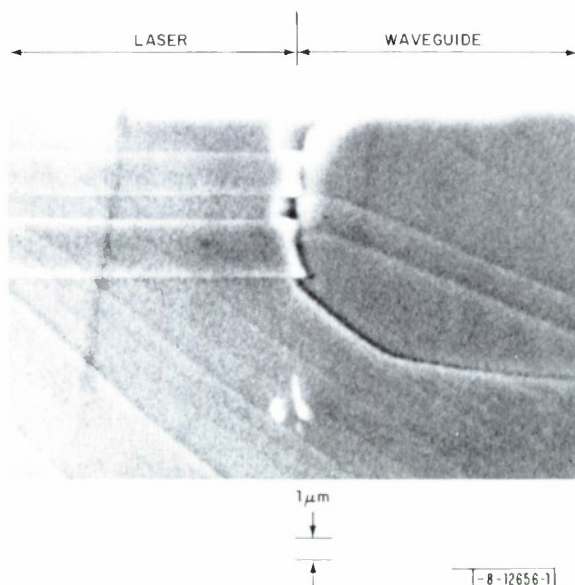


Fig. 1-2. Scanning electron micrograph of cleaved cross section of interface between GaAs-AlGaAs DH laser and high-purity GaAs waveguide. GaAs has been selectively etched about 0.3 μm after cleaving to enhance details. Diagonal lines and slight chipping at interface between laser active region and waveguide are both due to imperfect cleaving. (Cleavage plane is 45° to plane of interface.)

A scanning electron micrograph of a cross section of the laser-waveguide interface is shown in Fig. 1-2. It can be seen that the GaAs waveguide material makes intimate contact with the thin SiO_2 layer on the wall of the mesa. The apparent gap between the GaAs active region and the waveguide is the result of an imperfect cleave as well as the effect of the selective GaAs etch used after cleaving to enhance the definition of the various layers.

[†] A plane-wave calculation of the transmission properties at 9100 \AA of a layer of SiO_2 sandwiched between GaAs gives a reflectivity of >33 percent for a thickness t in the range 750 \AA < t < 2375 \AA .

Contact to the tops of the mesas was made with sputtered Cr-Au, and an alloyed Au-Sn contact was made to the substrate. The wafer then was sawed into dice 0.45 mm wide by 1.0 mm long, with the laser located near one end of the die. The lasers were pressure-contacted and tested using low-duty-cycle rectangular current pulses of 100-nsec duration. All measurements reported here were made with the devices at room temperature.

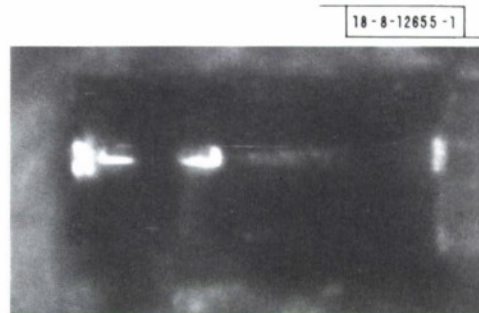
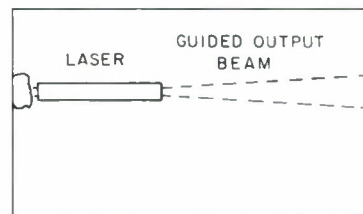


Fig. I-3. Infrared photomicrograph and artist's sketch of top view of operating integrated laser-waveguide structure. Laser itself is $45 \times 305 \mu\text{m}^2$. Brightness around diode perimeter is exaggerated by long exposure necessary to show up scattered light from beam. Bright spot at left-hand edge is due to scattering of beam by large chip in edge.



Above threshold, the laser radiation clearly was coupled into the waveguide and emitted from the waveguide layer at the end faces of the dice. An infrared photomicrograph of a top view of an operating laser-waveguide structure is shown in Fig. I-3. The path of the beam is evident due to scattering of some radiation out of the waveguide by surface imperfections. The light leaking out around the perimeter of the diode appears much more intense than it actually is because of the long photographic exposure required to show the light scattered from the confined beam.

For diodes which appeared to exhibit the expected conventional two-mirror Fabry-Perot operation, the spacing of the observed spectral modes was about 3 \AA , which corresponds to the calculated separation of the longitudinal modes of the $300\text{-}\mu\text{m}$ -long mesa (assuming an effective refractive index of 4.5). The lowest measured threshold current density for these lasers was 7.5 kA/cm^2 for the $1\text{-}\mu\text{m}$ -thick active region. The measured external differential quantum efficiencies of the laser-waveguide combination were somewhat low, about 3.5 percent. This may be the result of difficulties in collecting all the radiation emitted from the rough sawed end of the waveguide and/or the presence of internally reflected circulating modes¹⁴ which trap some of the energy within the laser. A rough measurement of the waveguide attenuation in these structures gave an upper limit of 8 cm^{-1} , a value which is higher than the 2 cm^{-1} of good high-purity GaAs waveguides⁵ at 9030 \AA but not high enough to significantly affect the external quantum efficiency.

A number of the diodes fabricated were not so well behaved as those described above. The operation of most of these devices, particularly the wider ones, appeared to be dominated by

total-internal-reflection modes. The observation of unusually low thresholds (as low as 3.5 kA/cm^2), low efficiencies ($\ll 1$ -percent external differential quantum efficiency), complex spectra, and emission from the corners of the mesas all are consistent with the presence of internally reflected modes.¹⁴ This is not too surprising since the etched side walls, as well as the ends of the lasers, were reflecting, and nothing was done to spoil the Q of the transverse cavity.

It is expected that considerable improvement in the performance of these integrated lasers can be obtained by the incorporation of a stripe-geometry structure to spoil the transverse Q and quench the internally circulating modes, as well as by reduction of the active region thickness to achieve lower threshold operation.

C. E. Hurwitz C. M. Wolfe
 J. A. Rossi G. E. Stillman
 J. J. Hsieh

B. SELENIUM ION-IMPLANTED GaAs

In our last report,¹⁵ we presented some preliminary results on the electrical characteristics of Se ion-implanted GaAs. In this section, we will present additional results including profiles of the electron carrier concentration vs depth of the samples reported in Ref. 15 and the variation of sheet carrier concentration with ion dose for samples annealed at 900° and 950°C .

The GaAs substrates used in these experiments were Cr-doped semi-insulating GaAs. After polishing and etching, a 500- to 700-Å layer of Si_3N_4 was pyrolytically deposited at 720°C on each sample. Details of this pyrolytic Si_3N_4 process can be found in a previous report.¹⁶ Recent Schottky barrier experiments¹⁶ on n-type test samples have indicated that this encapsulation technique is useful to anneal temperatures of at least 1000°C without failure of the Si_3N_4 or deterioration of the GaAs.

The 400-keV Se^+ ions were implanted through the Si_3N_4 overcoating at substrate temperatures ranging from room temperature to 500°C . After implantation, a 2000-Å pyrolytic SiO_2 layer usually was deposited at 400°C over the Si_3N_4 . The SiO_2 is not necessary for effective encapsulation, but protects the thin Si_3N_4 from scratching and other mechanical damage during handling. Anneals were then carried out in a flowing N_2 atmosphere at either 900° or 950°C for 15 minutes. The SiO_2 and Si_3N_4 layers were then removed in HF (about 6 minutes are required to remove a 700-Å layer of Si_3N_4). To minimize contact effects while carrying out Hall measurements of the van der Pauw type,¹⁷ electrically isolated cloverleaf-shaped mesas were defined in the implanted layer using 6000 Å of pyrolytic SiO_2 as an etch mask. Good linear contacts were obtained by alloyed Au-Sn. More complete details of the sample processing steps can be found in Ref. 16.

To determine the effects of implant temperature on the electrical activities of selenium, Se ions were implanted into GaAs samples at room temperature, 250° , 350° , and 500°C . Each sample was implanted with 1×10^{14} Se ions/ cm^2 and annealed at 900°C . The measured sheet carrier concentrations and sheet resistivities of these experiments were presented in Ref. 15. For the room-temperature implant, the sheet carrier concentration was $1.03 \times 10^{13} \text{ cm}^{-2}$. For the 250°C implant, this increased to $4.06 \times 10^{13} \text{ cm}^{-2}$, and further increased to $4.70 \times 10^{13} \text{ cm}^{-2}$ for the 350°C implant and to $4.99 \times 10^{13} \text{ cm}^{-2}$ for a 500°C implant. Based on estimates of the total implanted layer thickness,¹⁶ it was suggested that an increased depth (due to diffusion) with increased implant temperature might explain the increase in sheet carrier concentration from

$4.06 \times 10^{13} \text{ cm}^{-2}$ to $4.99 \times 10^{13} \text{ cm}^{-2}$ as the implant temperature was increased from 250° to 500°C . As described below, however, it has been found that the peak carrier concentration in these implanted layers also increased with implant temperature.

The variation of carrier concentration and mobility with depth for these GaAs implanted samples is shown in Figs. I-4 and I-5, respectively. These measurements were obtained from a series of etching steps and Hall measurements.^{16,18,19} (Note: all the data points have not been included in Figs. I-4 and I-5 for clarity.) For the room-temperature implant, the Se near the surface is either not electrically active or is compensated. The peak carrier concentration is $1.3 \times 10^{18} \text{ cm}^{-2}$ and occurs at a depth of $0.175 \mu\text{m}$ (1750 \AA). The samples implanted at 250° , 350° , and 500°C have peak carrier concentrations at depths of 700 to 800 \AA . These depths are close to the theoretical range from LSS theory,^{20,21} taking into account that the implants were made through 500 to 700 \AA of Si_3N_4 . The peak carrier concentration increased with implant temperature, and was about $2.0 \times 10^{18} \text{ cm}^{-3}$ for the 250°C implant, $3.0 \times 10^{18} \text{ cm}^{-3}$ for the 350°C implant, and $3.5 \times 10^{18} \text{ cm}^{-3}$ for the 500°C implant. The carrier concentration of all these samples decreases with depth more slowly than expected from LSS theory. Differences in this falloff with increasing depth down to about 10^{17} cm^{-3} are most likely due to differences in the thicknesses of the Si_3N_4 overcoatings and/or slight errors in the depth measurements. Below about $5 \times 10^{16} \text{ cm}^{-3}$, deeply penetrating tails which increase with implant temperature are observed. The extent of these deeply penetrating tails may be observed more clearly from

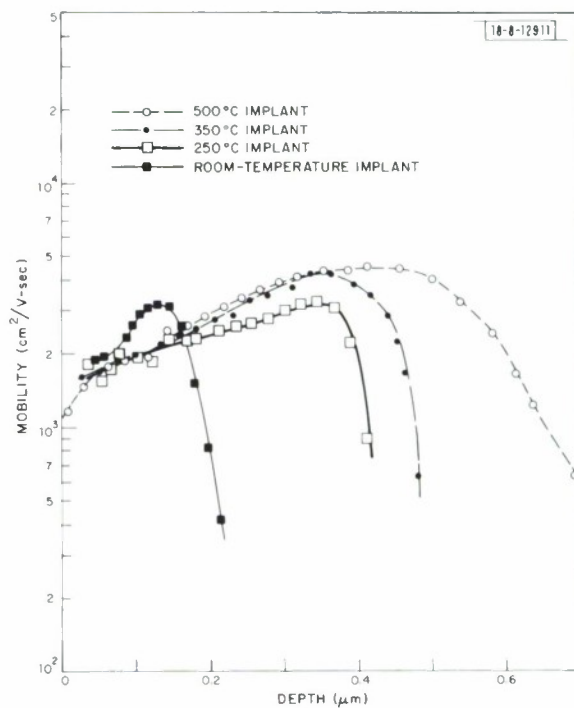
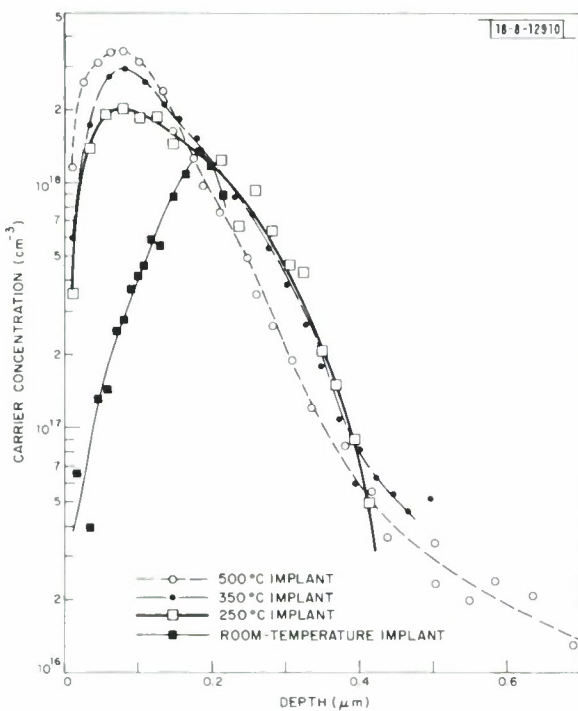


Fig. I-4. Carrier concentration vs depth measured in GaAs implanted at room temperature, 250° , 350° , and 500°C with 400-keV Se ions through 700 \AA of Si_3N_4 .

All samples were implanted with $1 \times 10^{14} \text{ Se/cm}^2$ and annealed at 900°C .

Fig. I-5. Mobility vs depth of sample whose carrier concentration is shown in Fig. I-4.

the mobility data (Fig.1-5). For the hot implants, the mobility is about 1800 to 2000 $\text{cm}^2/\text{V}\text{-sec}$ at the peak of the carrier concentration. The mobility on each sample increases as the carrier concentration decreases with increasing depth. For the 250°C implant, the mobility reaches a peak of about 3500 $\text{cm}^2/\text{V}\text{-sec}$ before decreasing rapidly with depth. This rapid decrease in mobility is probably associated with compensation effects of the Cr-doped substrate. The depth at which this mobility decrease occurs gives a good indication of the extent of the deeply penetrating tails. For the 350° and 500°C implants, the mobility increases to over 4000 $\text{cm}^2/\text{V}\text{-sec}$ before decreasing in the tails of the carrier concentration distribution. For the room-temperature implant, the mobility increases to about 3000 $\text{cm}^2/\text{V}\text{-sec}$ at a depth of about 0.13 μm , which is slightly shallower than the depth of the peak carrier concentration.

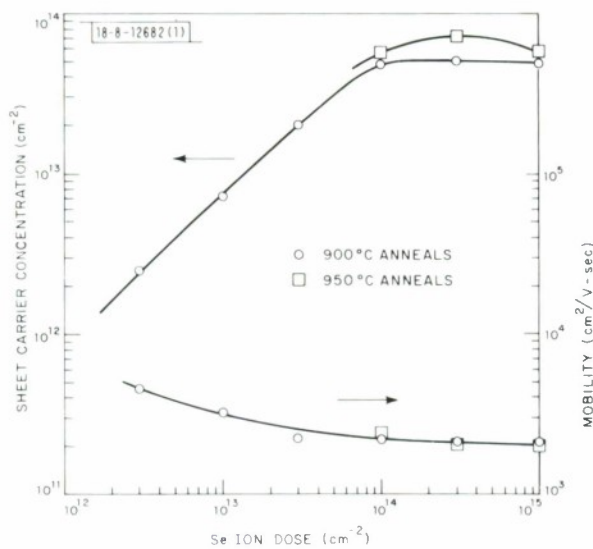


Fig.1-6. Sheet carrier concentration and mobility of GaAs layers implanted with 400-keV Se^+ ions at 350°C through 700 Å of Si_3N_4 .

To obtain representative information on the sheet carrier concentration as a function of ion dose, a series of implants were performed with the GaAs samples held at 350°C during implantation and annealed at either 900° or 950°C. Figure 1-6 shows the measured sheet carrier concentration and sheet mobility vs ion dose. For a dose of 3×10^{12} Se ions/ cm^2 (900°C anneal), the measured sheet carrier concentration was 2.5×10^{12} cm^{-2} , indicating that at least 80 percent of the Se ions have penetrated the Si_3N_4 coating and have been electrically activated in the GaAs. For the samples annealed at 900°C, the sheet carrier concentration increases with dose and saturates about 5×10^{13} cm^{-2} for doses above 10^{14} cm^{-2} . For samples annealed at 950°C, the sheet concentration reaches a maximum of 7×10^{13} cm^{-2} ($\rho_s = 44 \Omega/\square$) for a dose of 3×10^{14} cm^{-2} . The sheet mobility decreased from about 4600 $\text{cm}^2/\text{V}\text{-sec}$ for a Se dose of 3×10^{12} cm^{-2} , to 2100 $\text{cm}^2/\text{V}\text{-sec}$ for doses greater than 10^{14} cm^{-2} .

J. P. Donnelly
W. T. Lindley

C. GAIN PROFILE IN EXTERNAL CAVITY CONTROLLED GaAs LASERS

To reduce the relatively large emission bandwidth and the large beam divergence found in most III-V compound diode lasers, several workers have utilized the operation of diodes in an external cavity. By this method, some control over the longitudinal or transverse (or both)

mode pattern is obtained; this has already proven useful for some applications. Here we describe results which were obtained by operating GaAs heterostructure lasers in an external cavity. Specifically, the gain profile was measured for single (SH)-, double (DH)-, and large-optical-cavity (LOC) heterostructures with different active region dopants and under different device operating conditions.

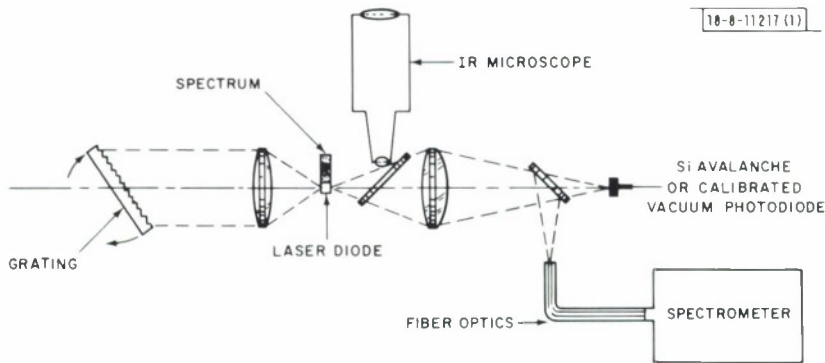


Fig. 1-7. Schematic illustration of external cavity and associated detection apparatus used in this work.

To map the gain profile for a device, a single-ended, dispersive external cavity was used. In this arrangement (described previously²² and shown here schematically in Fig. 1-7), light emitted from a cleaved, AR-coated face is collimated by a lens and dispersed by a diffraction grating. The diode light is re-imaged in the focal plane of the lens, but spatially dispersed so that only a small wavelength interval is reincident on the diode active region for amplification and lasing. By rotating the grating, the feedback wavelength and hence the lasing wavelength can be changed. For spectral measurements, the emitted light was analyzed by a 1-m spectrometer (resolution $\sim 0.2 \text{ \AA}$). The infrared microscope shown in Fig. 1-8 was used for cavity alignment as well as for observations of the lasing pattern on the diode facet. Throughout this work, the diodes were operated at or above room temperature and were driven by a low-duty-cycle ($f \sim 100 \text{ Hz}$) rectangular current pulse 100 nsec long with a rise time of less than 1 nsec.

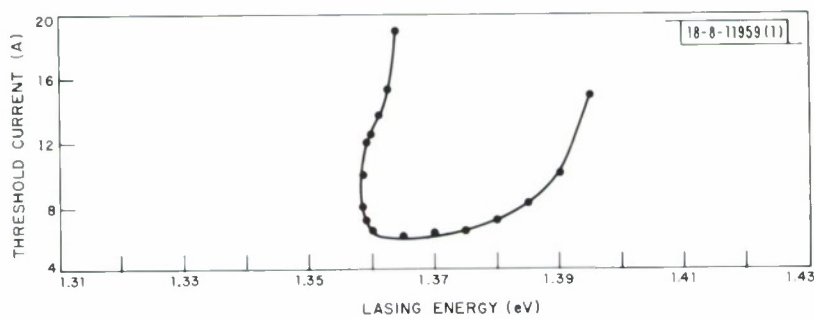


Fig. 1-8. Threshold current vs lasing energy for typical SH diode operated pulsed (100 nsec) at room temperature. (If current pulse is only 50 nsec, left-hand branch of curve is rotated clockwise.)

Figure 1-8 shows the curve of threshold current vs lasing energy, or gain profile, for a SH device operated at room temperature. The data were obtained by aligning the grating for operation at a certain photon energy $h\nu$ and increasing the current until lasing occurred. The grating was then rotated and the procedure repeated. For $h\nu < 1.365$ eV, the curve is double-valued. For example, if the grating is lined up to operate at $h\nu = 1.360$ eV and the current is increased, lasing begins at ~ 6 A and stops at ~ 13.5 A. This feature is characteristic of all SH diodes we have examined.

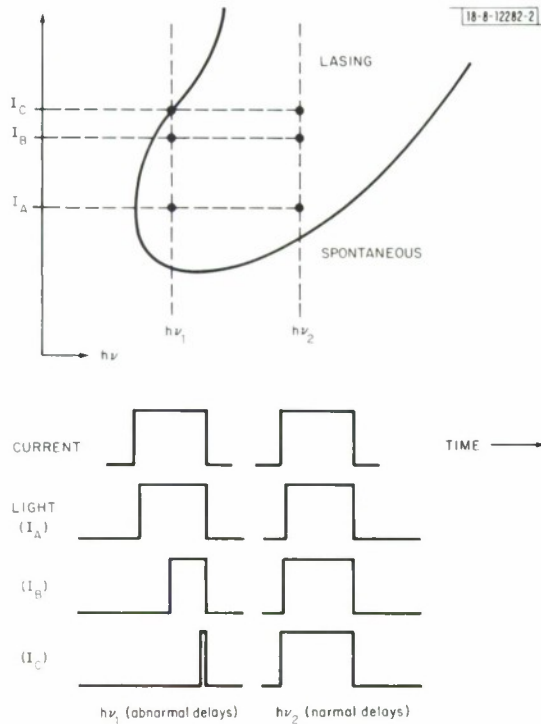


Fig. 1-9. Schematic of SH gain profile showing light output vs current ($I_A < I_B < I_C$) when diode is lased at $h\nu_1$ or $h\nu_2$. For lasing at $h\nu_1$, delay increases with increasing current (abnormal delay effect), whereas at $h\nu_2$, time delay behavior is normal. Change in amplitude of light output is not indicated.

Figure 1-9 shows schematically the time dependence of the laser emission from these SH diodes. With the grating set to provide feedback at energy $h\nu_2$, the light output pulse for three rectangular current pulses of different amplitudes ($I_A < I_B < I_C$) is shown by the right-hand portion of the figure. In this case, the light output follows the current, and little or no delay is observed. The amplitude of the light output increases as the current amplitude is increased (this is not indicated in the figure). If the grating is lined up to operate at $h\nu_1$, then as the current amplitude is increased a significant delay develops between the current pulse and the light output pulse, until at I_C the light pulse is delayed almost to the end of the current pulse. For $I > I_C$, only spontaneous emission is observed. Thus, the gain profile is comprised of two portions: a lower energy portion, characterized by a delay that increases with increasing current, i. e., an abnormal delay region; and a higher energy portion characterized by normal time behavior. At high injection levels, the abnormal region monotonically moves into the higher energy portion.

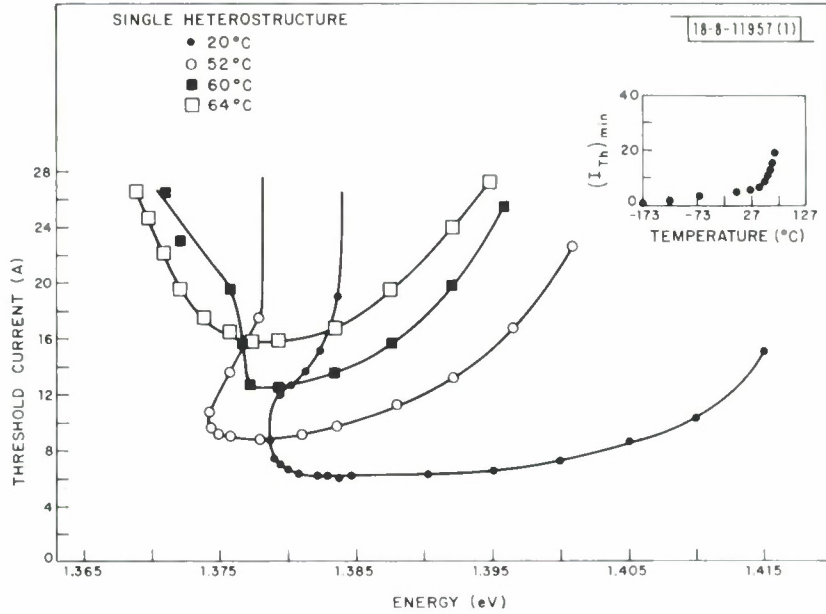


Fig. 1-10. Variation in SH gain profile with temperature. Note that abnormal delay region (where lasing stops at sufficiently high currents) is eliminated at higher temperatures. Inset shows plot of minimum threshold current $(I_{th})_{min}$ needed for lasing at several different temperatures.

Figure 1-10 shows the gain profile for another SH at several different operating temperatures. At 20°C, the profile is similar to that shown in Fig. 1-8, having a "toe" region with abnormal delays and a region without these effects at higher energies. When the temperature is increased to 52°C, the entire curve shifts to higher currents and lower energy, as expected, but the low-energy portion moves only slightly, while the high-energy portion moves faster. The net effect is a significant decrease in the tuning width. Increasing the temperature to 60°C continues this trend and, in addition, causes the "toe" region to disappear. At this temperature, a significant delay between the current pulse and the light output (20 to 30 nsec at $I \approx 1.5 I_{th}$) is observed over the entire profile; however, this delay is "normal," since it does not increase with increasing current. In fact, in this temperature range the behavior of these diodes is typical of uncoated SH diodes as their temperature of operation approaches the transition temperature.^{23,24} A further increase in the temperature to 64°C results in a more symmetric gain profile and in an increase in the delay to about 40 to 50 nsec measured at $1.5 I_{th}$. In summary, as the temperature is increased, the gain profile moves to lower energy, the abnormal delay region disappears, and a long delay is observed over the entire profile.

By examining the external cavity data, it is possible to predict the behavior of an uncoated diode. For example, in Fig. 1-10 there is a minimum threshold current $(I_{th})_{min}$ at each temperature. If we plot $(I_{th})_{min}$ vs T for these and several other temperatures, we obtain the data shown in the inset. These data are obviously similar to reported data^{23,24} for the variation of I_{th} with temperature for SH and DJ (diffused junction) devices: $(I_{th})_{min}$ increases sharply as T_c is approached. As another example, if we assume that an uncoated diode would lase at the energy for which $(I_{th})_{min}$ occurs, it follows that the rate of change of the lasing energy with temperature will first be negative, then approach zero and perhaps even become positive, and finally be increasingly negative as $T \rightarrow T_c$, in qualitative agreement with the data in Ref. 25.

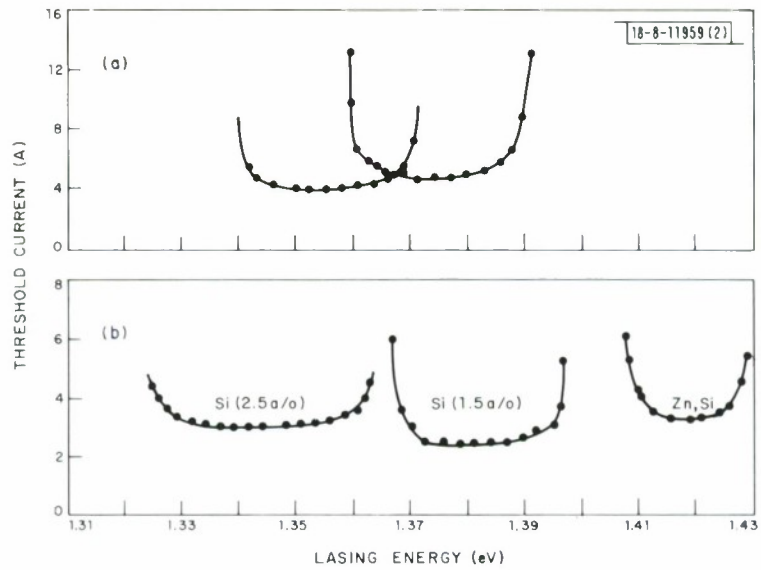


Fig. I-11. Gain profiles for (a) LOC and (b) DH devices. Note more symmetric appearance when compared with SH gain profile (Fig. I-8). Different gain profiles were obtained by changing active region dopant.

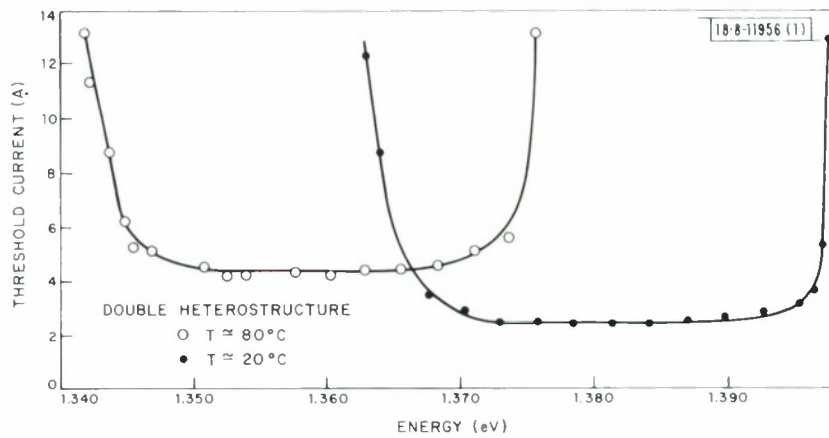


Fig. I-12. Variation in DH gain profile with temperature. Whole profile shifts to lower energy with increasing temperature at rate ~ -0.4 meV/ $^{\circ}$ C.

In Fig. I-11(a-b), we show the gain profiles for LOC and DH devices operated at room temperature. For these structures, the gain profiles are fairly symmetric around a center energy which depends on the active region dopant. Diodes from two different LOC wafers were measured. The gain profile centered at 1.375 eV was obtained for diodes made from a wafer whose active region was doped with both Zn and Si. The profile centered at ~ 1.355 eV was obtained for diodes with only Si doping in the active region. For DH diodes, changing from Zn and Si doping of the active region to heavy Si doping (1.5 atomic percent Si in the solution used to grow the active layer) both broadens the tuning curve and shifts the centroid of the curve to a lower energy. Even heavier Si doping (2.5 atomic percent Si in the solution) continues this trend, yielding diodes which may be continuously tuned over a 40-meV (300-Å) range.

For LOC or DH lasers, there are no regions of the gain profile where the diode stops lasing as the current is increased. Also, for these structures, as the temperature is increased the whole tuning curve shifts to lower energy at a rate of ~ -0.4 meV/°C, as shown in Fig. I-12. This rate is in good agreement with the reported shift of the bandgap with temperature.²⁶

J. A. Rossi
 J. J. Hsieh
 H. Heekseher

D. PbS MIS DEVICES FOR CHARGE-COUPLED INFRARED IMAGING

Results of an experimental investigation of PbS MIS devices suggest, for the first time, the feasibility of developing a monolithic two-dimensional charge-coupled imaging device (CCID) in a narrow-gap semiconductor which would be operable at 77 K and have moderate sensitivity out to about 3.5 μm .^{27,28} The PbS MIS devices have been fabricated from Bridgman-grown crystals using wafers which had been two-zone annealed to achieve p-type carrier concentrations in the 5×10^{16} to 3×10^{17} cm^{-3} range. (The former concentration is the lowest presently available.) The crystals have 77 K mobility of $\sim 10^4$ $\text{cm}^2/\text{V-sec}$ and are homogeneous, as indicated by their high thermoelectric power (520 to 400 $\mu\text{V}/\text{K}$).

The wafers are mechanically polished prior to annealing. Devices are fabricated by first etching each sample in aqua regia at 40°C and then pyrolytically depositing typically 2000 Å of SiO₂ at 400°C in a hot stage by the reaction of SiH₄ and O₂ in a N₂ atmosphere. Layers of Ti (~ 500 Å) and Au (~ 1 μm) then are sequentially sputtered over the oxide.

By using standard photolithographic techniques, 15-mil-square devices are defined which have 5-mil-diameter electroplated-In bonding pads. The back of the chip is plated with Au and then In to form a large-area contact. Finally, the chip is attached to a header, the device is bonded manually, and the header is mounted on the cold finger of a liquid N₂ dewar. The dewar is equipped with a cold shield so that measurements could be made in an ~ 85 K background.

Figure I-13 shows the capacitance-voltage (C-V) characteristics at 77 and 300 K, with frequency as a parameter, of a typical device fabricated on p-type material with a surface concentration of 2.6×10^{17} cm^{-3} . For frequencies greater than 5 kHz, measurements were made with a variable-frequency capacitance bridge; below 5 kHz, a phase-sensitive detection scheme utilizing a two-phase lock-in amplifier was employed. The 300-K curves have low-frequency behavior and indicate that the PbS surface is depleted at zero bias and that the surface potential can be varied with bias from accumulation through inversion. At 77 K, the thermal generation rate is much reduced and the electrons in the surface inversion layer cannot follow the AC signal, so that high-frequency behavior is observed. The shift of the oxide capacitance with

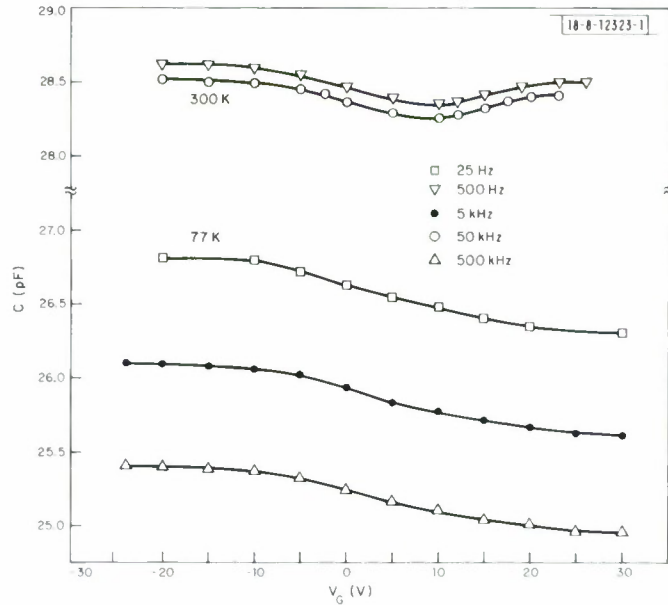


Fig. I-13. C-V characteristics at 300 and 77 K for p-type PbS MIS device over frequency range of 25 Hz to 500 kHz. Variation of oxide capacitance with temperature and frequency accounts for vertical shift of curves.

temperature is characteristic of our pyrolytic oxides, and also has been observed on silicon-pyrolytic SiO_2 -metal devices we have fabricated. The shift of capacitance with frequency at 77 K is due to a logarithmic frequency dependence of the oxide dielectric constant, and will be discussed further below.

Both the 77- and 300-K C-V curves are consistent with theoretical C-V characteristics for PbS MIS devices. In contrast to Si MOS devices, the variation of capacitance with bias is very small and occurs over a relatively large voltage range. These differences are due to the high PbS carrier concentration and large static dielectric constant of 181 at 77 K, which result in a depletion capacitance of $\sim 10^{-6}$ F/cm² and an oxide electric field of $\sim 10^6$ V/cm to achieve inversion.

At 77 K, the oxide is characterized by a relative dielectric constant of 4.33 at 10 kHz and a breakdown strength of 3.5×10^6 V/cm. Since the capacitance transient measurements to be discussed below show no semiconductor avalanche up to 50 V bias, these oxide parameters indicate that present PbS MIS devices have a charge-storage capacity in excess of 2×10^{12} electrons/cm² (3.2×10^{-7} C/cm²). Here, the storage capacity is defined as the equilibrium number of minority carriers in the surface inversion layer for each bias and has been calculated from the solution of the Poisson equation using Fermi-Dirac statistics, since the range of surface potentials of interest corresponds to the weakly degenerate region.

Figure I-14(a-b) shows C-V and conductance-voltage (G-V) data as a function of frequency at 77 K for another device fabricated on the same chip. Here, the measured capacitance has been normalized with respect to the oxide capacitance; the dispersion at large bias is due to the frequency dependence of the oxide dielectric constant. The measured conductance is plotted as

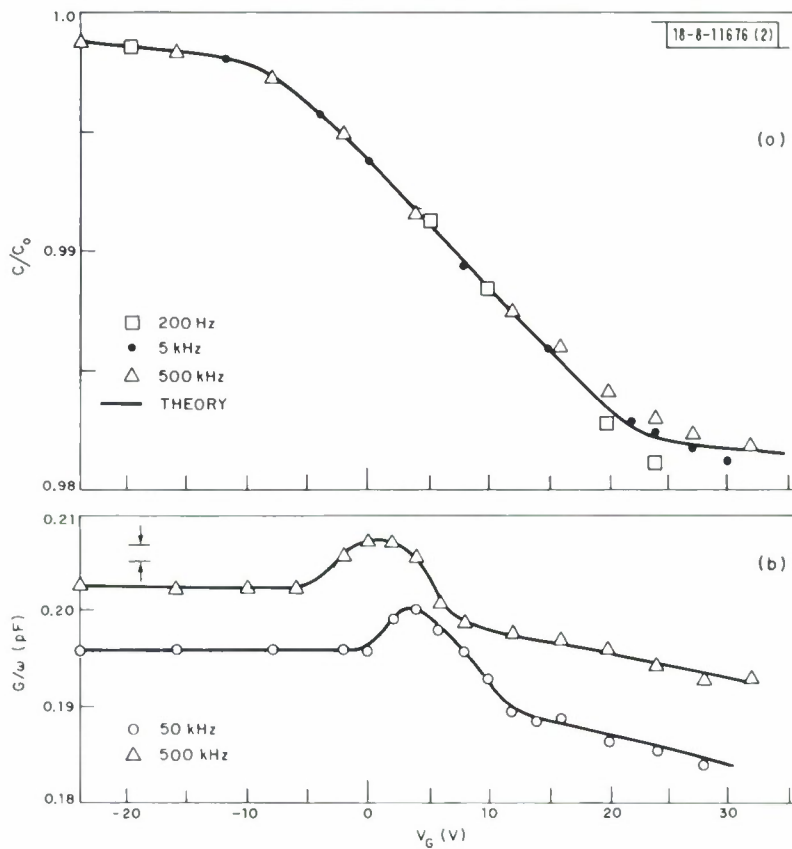


Fig. 1-14. (a) Experimental and theoretical normalized C-V characteristic for p-type PbS MIS device at 77 K over frequency range of 200 Hz to 500 kHz. Uncertainty in measured capacitance corresponds to size of data points. (b) Experimental C-V plots of same device measured at 50 and 500 kHz at 77 K. Conductance has been normalized with respect to ω ($=2\pi F$). Uncertainty in conductance measurement is indicated by error bars.

G/ω and scales nearly linearly with frequency. The curves are characterized by a small conductance peak, associated with interface state loss, which is superimposed on a background conductance due to the AC conductivity of the oxide.

The frequency dependence of the oxide conductance and capacitance is a bulk property of the pyrolytic SiO_2 . This was determined by fabricating and measuring a set of metal-insulator-metal capacitors with different oxide thicknesses. A frequency-dependent conductivity is characteristic of many deposited thin-film insulators.²⁹ Moreover, it can be shown by the Kramers-Kronig relation that a conductivity linearly dependent on frequency implies that the real part of the dielectric constant varies logarithmically with frequency.

By including the oxide conductance in the equivalent circuit model for an MIS device, it is possible to fit theoretically the 77-K C-V and G-V data.³⁰ One finds that the measured capacitance can be well approximated by the series combination of the oxide capacitance and that of the PbS depletion layer since the interface state capacitance is effectively masked by the large PbS depletion capacitance. In Fig. 1-14(a), the data have been fitted with such a theoretical curve for an oxide thickness of 2020 Å and a flat-band voltage of -12 V. With the circuit model, the conductance peak due to interface state loss can be extracted from the background conductance.

The resulting peak can be fitted by a model that includes a continuum of states across the band-gap and accounts for surface-potential fluctuations at the semiconductor-oxide interface.³¹ The small size of the peak relative to the background is attributable to the large PbS depletion capacitance. Analysis of G-V data for several samples yields estimates of the interface state density of $1.2 \times 10^{12} \text{ cm}^{-2} \text{ eV}^{-1}$ and capture cross section of $1 \times 10^{-15} \text{ cm}^2$.

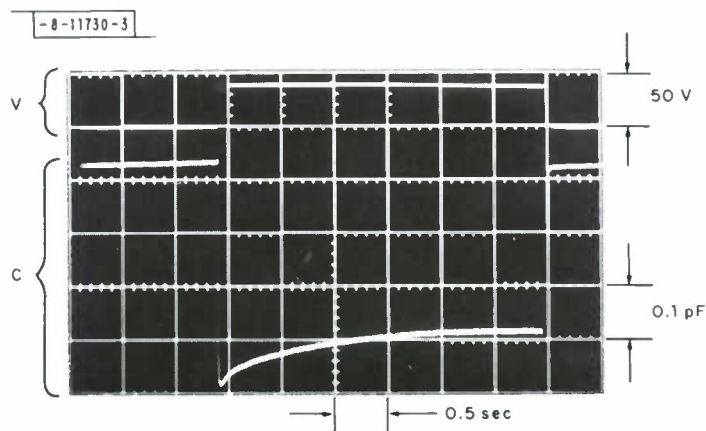


Fig. 1-15. Dual-beam oscilloscope traces showing applied voltage pulse and resulting capacitance transient in 85-K background for PbS MIS device initially biased at 0 V for voltage pulse of 40 V.

Storage-time measurements were made by pulsing a device with a voltage sufficient to invert the surface and monitoring both the voltage pulse and the capacitance transient (as the analog output of a capacitance meter) on a dual-beam oscilloscope. A typical trace, from measurement in an 85-K background, is shown in Fig. 1-15: for a voltage pulse which shifts the bias from 0 to 40 V, the capacitance drops from its zero-bias value to its deep-depletion value and then slowly rises to a final point determined by the bias. The storage time is defined as the duration of this capacitance transient. On this device, the transient has decayed to 10 percent of its initial value in 1.7 sec. The total duration of the transient, as shown in the figure, is approximately 2.3 sec, nearly two orders of magnitude longer than the 1/30-sec frame time for standard two-dimensional imaging; it is this result that suggests the feasibility of a two-dimensional PbS CCD. Analysis of such transients³⁰ suggests that the equilibration is controlled by depletion-layer thermal generation which is characterized by a generation lifetime of 2×10^{-10} sec.

The measured deep-depletion capacitance is consistent with calculated values. Moreover, increasing the voltage pulse amplitude results in lower values of deep-depletion capacitance, indicating that avalanche fields have not been reached, at least for the 50-V pulses that have been used. If a voltage pulse smaller than is needed to invert the surface is applied, the capacitance curve has the expected step function shape.

Calculations of charge transfer efficiency for a two-phase overlapping-gate PbS CCD using the MIS parameters determined in this study indicate that good transfer characteristics should be achievable under fat-zero operation. Utilizing expressions for transfer efficiency developed by Tompsett,³² and assuming lengths of 25 and 8 μm for the storage and transfer gates, respectively, one calculates in the small-signal limit a total transfer inefficiency of $\sim 4 \times 10^{-5}$ per transfer for a fat zero of 5×10^{11} electrons/cm², corresponding to about 25 percent of a full well, with the variable-transfer-time effect the dominant source of inefficiency.

The imaging sensitivity of a PbS CCID probably will be controlled by the uniformity of response that can be achieved. For instance, with a fat zero of 5×10^{11} electrons/cm², a 5-percent nonuniformity over the CCID implies that a photon flux corresponding to a signal packet of 2.5×10^{10} electrons/cm² could be detected at a signal-to-noise ratio of 1. Even greater sensitivity could be attained by using frame-to-frame subtraction, which possibly could be done on an adjacent Si CCD chip.³³ These sensitivity considerations also would apply to other imaging schemes in PbS suggested by the results reported here, such as an array of charge-injection devices or a buried-channel CCID. The latter device could be fabricated using ion-implantation techniques³⁴ to form the shallow junction, and in low-background applications should provide greater imaging sensitivity than a surface-channel device since it could operate with a smaller fat zero.

F. J. Leonberger
A. I. McWhorter
T. C. Harman

REFERENCES

1. Y. Suematsu, M. Yamada, K. Hayashi, K. Furaya, and S. Ibukuro, presented at the 1974 IEEE International Laser Conference, Atlanta, Georgia, 18-20 November 1974; Y. Suematsu, M. Yamada, and K. Hayashi, Proc. IEEE 63, 208 (1975).
2. F. K. Reinhart and R. A. Logan, Appl. Phys. Lett. 25, 622 (1974).
3. D. R. Scifres, R. D. Burnham, and W. Streifer, Appl. Phys. Lett. 25, 203 (1974); D. B. Anderson, R. R. August, and J. E. Coker, Appl. Opt. 13, 2742 (1974); H. M. Stoll and D. H. Seib, Appl. Opt. 13, 1981 (1974); M. Nakamura, K. Aiki, Jun-ichi Umeda, A. Yariv, H. W. Yen, and T. Morikawa, Appl. Phys. Lett. 25, 487 (1974).
4. S. Wang, IEEE J. Quantum Electron. QE-10, 413 (1974).
5. G. E. Stillman, C. M. Wolfe, J. A. Rossi, and H. Heckscher, unpublished data.
6. F. K. Reinhart, Appl. Phys. Lett. 22, 372 (1973).
7. J. C. Dymont, F. P. Kapron, and A. J. Springthorpe, Proceedings of 5th International Symposium on GaAs and Related Compounds, Deauville, 1974 (Institute of Physics, London, to be published).
8. G. E. Stillman, C. M. Wolfe, J. A. Rossi, and J. P. Donnelly, Appl. Phys. Lett. 25, 671 (1974), DDC AD-A006705.
9. G. E. Stillman, C. M. Wolfe, A. G. Foyt, and W. T. Lindley, Appl. Phys. Lett. 24, 8 (1974), DDC AD-777559/6.
10. Y. Tarui, Y. Komiya, and Y. Harada, J. Electrochem. Soc. 118, 118 (1971).
11. A. S. Dobkin, V. V. Kokorov, G. A. Lapitskaya, A. A. Pleshov, O. N. Prozorov, L. A. Rivkin, G. A. Sukharev, V. S. Shil'dyaev, and S. D. Yakubovich, Sov. Phys.-Semiconductors 4, 515 (1970).
12. F. A. Blum, K. L. Lawley, F. H. Doerbeck, and W. C. Holton, Appl. Phys. Lett. 25, 620 (1974).
13. R. A. Logan and F. K. Reinhart, J. Appl. Phys. 44, 4172 (1973).
14. I. Hayashi and M. B. Panish, J. Appl. Phys. 41, 150 (1970).
15. Solid State Research Report, Lincoln Laboratory, M.I.T. (1975:1), p. 8, DDC AD-A009848.
16. Ibid., pp. 2-7.

17. L. J. van der Pauw, Philips Res. Rep. 13, 1 (1958).
18. J. D. Sansbury and J. F. Gibbons, Radiation Effects 6, 269 (1970).
19. J. M. Woodeoek, J. M. Shannon, and D. J. Clark, Solid-State Electron. 18, 267 (1975).
20. J. Lindhard, M. Seharff, and H. Schiott, Kgl. Danske Videnskab. Selskab, Mat. Fys. Medd. 33, 1 (1963).
21. W. J. Johnson and J. F. Gibbons, Projected Range Statistics in Semiconductors distributed by Stanford University Bookstore (1970).
22. J. A. Rossi, S. R. Chinn, and H. Heekseher, Appl. Phys. Lett. 23, 25 (1973), DDC AD-771902/4.
23. E. A. Ulmer and I. Hayashi, IEEE J. Quantum Electron. QE-6, 297 (1970).
24. M. J. Adams, S. Gründorfer, B. Thomas, C. F. L. Davies, and D. Mistry, IEEE J. Quantum Electron. QE-9, 328 (1973).
25. B. Thomas, D. Mistry, and C. F. L. Davies, IEEE J. Quantum Electron. QE-10, 401 (1974).
26. M. B. Panish and H. C. Casey, Jr., J. Appl. Phys. 40, 163 (1969).
27. This work was reported in preliminary form in the Solid State Research Report, Lincoln Laboratory, M.I.T. (1974:2), p. 1, DDC AD-783634/9, and at the Device Research Conference, Santa Barbara, California, 25-27 June 1974 (unpublished).
28. F. J. Leonberger, A. L. McWhorter, and T. C. Harman, Appl. Phys. Lett. 26, 704 (1975).
29. See, for example, A. K. Jonseher, J. Non-Crystalline Solids 8-10, 293 (1972).
30. F. J. Leonberger, "Lead Sulfide MIS Devices for Charge-Coupled Imaging Applications," Ph. D. Thesis, M.I.T. (1975)(unpublished).
31. E. H. Nicollian and A. Goetzberger, Bell Syst. Tech. J. 46, 1055 (1967).
32. M. F. Tompsett, IEEE Trans. Electron Devices ED-20, 45 (1973).
33. For one such scheme, see E. S. Kohn and M. L. Schultz, Technical Report AF-CRL-TR-74-0056, 1974 (unpublished).
34. J. P. Donnelly, T. C. Harman, A. G. Foyt, and W. T. Lindley, Solid-State Electron. 16, 529 (1973), DDC AD-763577.

II. QUANTUM ELECTRONICS

A. OPTICALLY PUMPED SEMICONDUCTOR LASERS

1. Long-Path Monitoring Techniques and Atmospheric Spectroscopy with InSb Laser

We have previously demonstrated that GaAs transverse-pumped InSb lasers are capable of Doppler-limited molecular absorption spectroscopy.¹ Now, we have laboratory tested the long-path propagation characteristics of these lasers in order to establish their utility as atmospheric pollution monitors. We have obtained diffraction-limited operation using the double-folded path shown in Fig. II-1. The divergent InSb laser beam emerging from the dewar is collimated by the 7.5-cm-diameter, 30-cm-focal-length spherical mirror M_C ; it then propagates to a folding mirror M_F , then to the corner-cube retroreflector M_R and retraces its path. The return beam is focused by M_C onto the photovoltaic InSb detector off the 50-percent beam splitter BS. This arrangement is similar to the optical geometry of Hinkley and Ku² except for the inclusion of the M_F . This mirror doubles the available path and permits single-ended alignment at the laser-retroreflector site. Alignment is accomplished with a He-Ne laser, in place of the retroreflector, directed at M_F to M_C , where it is focused on the sample and detector. The retroreflector is then uncritically inserted in front of the He-Ne laser to form the return path. The retroreflector's properties make alignment insensitive to its own, and to the folding mirror's, angular orientation. If the retroreflector is replaced with a flat mirror, both vibrations and air turbulence create detrimental alignment instabilities. A loss of ~20 percent was measured over a 40-m path, of which ~13 percent is calculated from diffraction-limited operation and the rest is due to the reflectivity loss from the M_F .

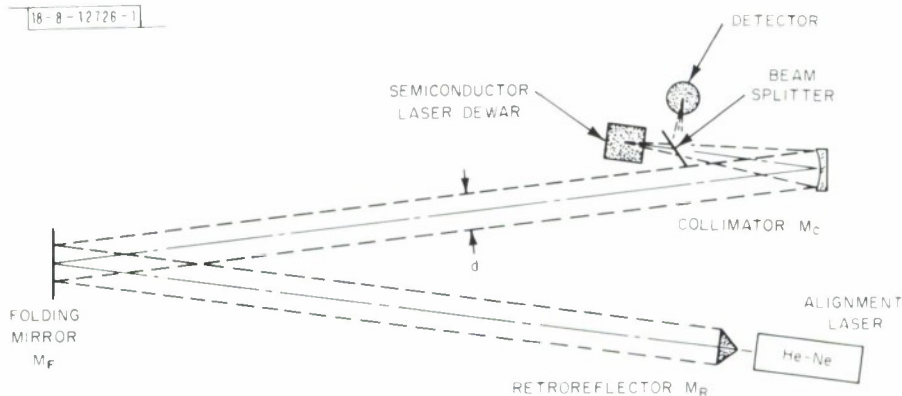


Fig. II-1. Double-folded long-path geometry for atmospheric monitoring with tunable semiconductor lasers.

A double-folded, ~7-m optical path has been used in conjunction with an InSb laser temperature tuned by ramp-scanning the injection current to the GaAs diode pump laser. The resultant absorption traces are given in Fig. II-2. The upper trace exhibits three sharp absorption lines due to atmospheric water vapor (laboratory humidity 42 percent, temperature 22°C); the steplike structure arises from laser mode jumps. In the second trace, we have inserted a 25-cm cell containing 1 Torr of NO; in the third, a 10-cm cell of C_2H_4 at 5 Torr; and in the fourth, a Ge etalon with a 0.13-cm^{-1} FSR for frequency calibration. The absorption lines of H_2O , NO, and C_2H_4 , which are produced in most combustion engines, are well separated, quite distinct and, as seen here, can be monitored with a single laser.

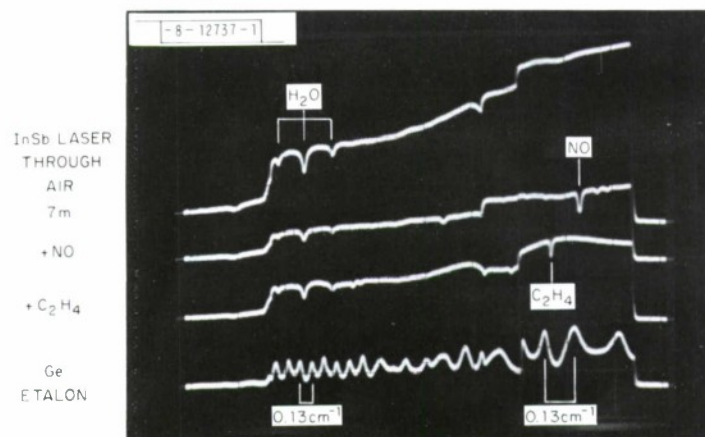


Fig. II-2. Real-time (~ 2 -nsec) absorption traces of nitric oxide (1 Torr, 25 cm), ethylene (5 Torr, 10 cm) and atmospheric water vapor (42-percent humidity, 22°C) taken with CW GaAs transverse-pumped InSb laser over 7-m double-folded path.

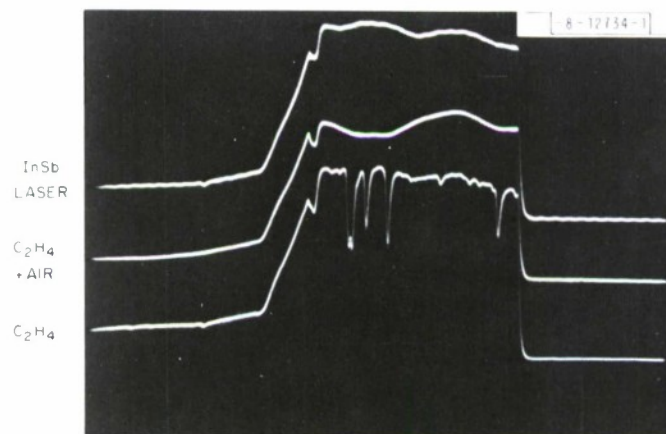


Fig. II-3. Real-time (~ 10 -nsec) absorption trace of ethylene (1 Torr in 7.3-m White cell) taken with CW GaAs transverse-pumped InSb laser.

Comparison with the etalon fringe spacing shows the low-pressure NO and C₂H₄ lines to be Doppler-limited. The water-vapor linewidths are much smaller than the usual atmospheric pressure-broadened widths ($\sim 0.1 \text{ cm}^{-1}$). Collisional narrowing of high rotational state H₂O lines which show weak rotational broadening has been studied recently by Eng *et al.*³

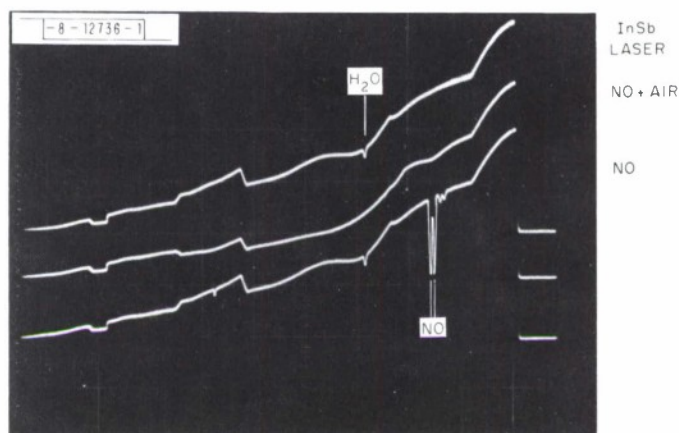


Fig. II-4. Real-time (~ 2 -msec) absorption trace of nitric oxide (0.1 Torr in 7.3-m White cell) taken with CW GaAs transverse-pumped InSb laser.

A 7.3-m multipass White cell was used to study C₂H₄ and NO in air. Figure II-3 shows transmission through (top) the evacuated White cell, (bottom) 1 Torr C₂H₄, and (middle) 1 Torr C₂H₄ in air. The middle trace shows the extreme loss of sensitivity due to pressure broadening. A similar set of traces is shown in Fig. II-4 where (top) the evacuated cell trace and (bottom) the 0.1-Torr NO trace exhibit a small dip due to residual water vapor in the cell. The well-resolved NO lambda doublet in the bottom trace indicates an instrumental resolution better than the Doppler limit. The broad absorption centered on the H₂O dip is due to water vapor in the 2-m air path outside the cell. The introduction of 1 atm of air into the cell increases the broad H₂O absorption while decreasing the NO absorption peak. The air-broadened spectra in Figs. II-3 and II-4 are comparable to those expected from auto exhausts, where NO and C₂H₄ concentrations are from 100 to 1000 ppm.

2. CW InAs Lasers Optically Pumped with GaAs Diode Lasers

We previously reported CW laser emission from InSb and InAs at ~ 4 K pumped with a Nd:YAG laser, and from InSb pumped with a GaAs diode laser. We now also have obtained CW InAs lasers pumped by GaAs diode lasers. The InAs lasers were cut from an n-type crystal ($n \sim 2.8 \times 10^{16} \text{ cm}^{-3}$) grown by Bell and Howell. Continuous operation was achieved with the samples mounted directly on the GaAs diode with thermal grease. Sample homogeneity for this InAs crystal was sufficient to permit such direct mounting with a high probability that either CW operation or long-pulse operation, sufficient for time-resolved spectroscopy, would be obtained.

The spectral region of InAs laser emission ($\sim 3 \mu\text{m}$) is an important one for pollution monitoring since several hydrogenic molecules including acetylene (C₂H₂) as well as ammonia (NH₃)

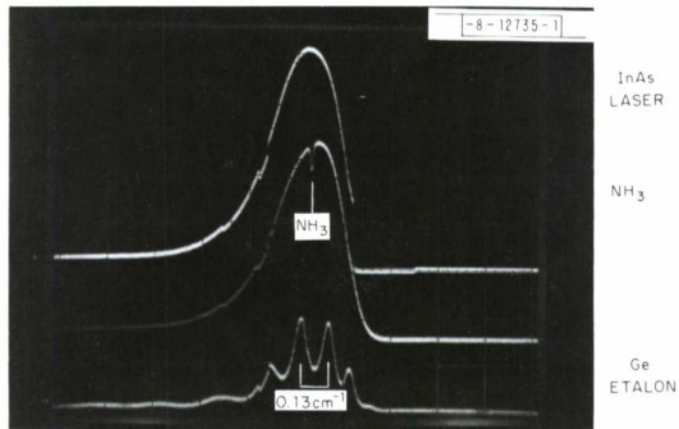


Fig. II-5. Tunable GaAs transverse-pumped InAs laser absorption spectrum of ammonia $\nu_p(P_1)$ line (2 Torr, 30 cm); real-time scan ~ 5 msec.

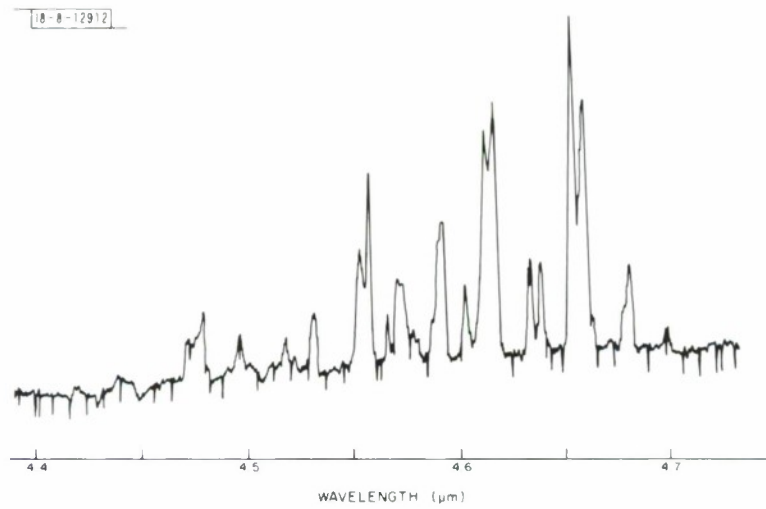


Fig. II-6. Spectrum of Bridgman-grown $\text{PbS}_{0.8}\text{Se}_{0.2}$ laser transverse-pumped with GaAs diode laser.

have absorption bands in this region. An NH_3 absorption at $3\ \mu\text{m}$ is given in Fig. II-5 which shows (top) an InAs laser emission trace, (middle) emission trace after passage through a 30-cm cell containing a 2-Torr NH_3 , and (bottom) emission through a 13-cm^{-1} FSR Ge etalon.

A study was made of the effect of magnetic field on the emission properties of the GaAs/InAs combination. Magnetic fields up to 9 kOe were applied parallel to the pump laser emission, perpendicular to the InAs emission. Over this field range there was no significant change in either the InAs laser threshold value or in the wavelength of InAs emission with varying magnetic field. This behavior is in marked contrast with the magnetic-field effects observed with the GaAs/InSb combination.¹ This difference in behavior is believed to be due to the larger exciton binding energy of InAs.

3. Diode-Pumped Pulsed Semiconductor Lasers

Attempts were made to obtain optically pumped laser emission from a number of other semiconductors using a GaAs diode laser as the pump source. The materials tested were GaSb and $\text{PbS}_{1-x}\text{Se}_x$ ($x = 0.4, 0.2, 0$). The GaSb sample was from an ingot supplied by Bell and Howell. It was p-type ($p \approx 1.1 \times 10^{17}\ \text{cm}^{-3}$) with polished (110) faces and cleaved ($1\bar{1}0$) edges. The $\text{PbS}_{0.8}\text{Se}_{0.2}$ and $\text{PbS}_{0.6}\text{Se}_{0.4}$ samples were from Bridgman-grown crystals made by A. J. Strauss; they were p-type ($p \sim 5 \times 10^{17}\ \text{cm}^{-3}$) with polished (100) faces and cleaved (010) edges. The similarly oriented PbS sample was from a vapor-grown ingot made by T. Harman; it was n-type ($n = 1 \times 10^{17}\ \text{cm}^{-3}$). Although CW operation was not obtained from any of these samples, pulsed-laser emission was achieved with all of them.

Of the samples tested, GaSb had the highest threshold ($\sim 1.5\ \text{W}$). Achieving this power level with the GaAs diode required injection currents of $\sim 3.5\ \text{A}$, which limited the length of the pump pulse to $\sim 1\ \mu\text{sec}$ because of heating. Under these pulse conditions, three longitudinal GaSb laser modes were observed, but with over 90 percent of the laser emission contained in a single mode at $1.549\ \mu\text{m}$.

The Bridgman-grown $\text{PbS}_{1-x}\text{Se}_x$ ($x = 0.2, 0.4$) samples investigated here had been optically pumped previously in an immersion dewar ($T \sim 2\ \text{K}$) by Q-switched Nd:YAG laser pulses 200 nsec wide with up to a few hundred watts power.⁴ Multimode emission with laser operation over broad-band widths up to $\sim 200\ \text{cm}^{-1}$ were observed. We have found that similar results can be obtained by pumping the samples with a GaAs diode laser in a cold-finger dewar ($T \sim 10\ \text{K}$) at power levels of $\sim 1\ \text{W}$, as seen in the emission spectrum of $\text{PbS}_{0.8}\text{Se}_{0.2}$ shown in Fig. II-6. The injection current to the GaAs pump diode to achieve the laser emission of Fig. II-6 was less than 1 A, and heating limited pulse lengths to $\sim 3\ \mu\text{sec}$.

Mooradian *et al.*⁴ obtained a similar broad-band spectrum from their Bridgman-grown sample of PbS. However, the vapor-grown PbS sample supplied by T. Harman showed the markedly narrower laser spectrum given in Fig. II-7. The threshold for laser emission in the PbS sample shown was $\sim 0.6\ \text{W}$, with internal sample heating limiting the pulse length to $\sim 10\ \mu\text{sec}$. This pulse length is disappointingly short, particularly in view of the fact that quasi-CW laser action has been obtained in InAs samples with similar threshold values. The difference is believed to be due largely to a lower heat-sinking efficiency with PbS because of its lower thermal conductivity and its greater thickness ($\sim 100\ \mu\text{m}$ vs $\sim 20\ \mu\text{m}$) necessitated by the more difficult polishing and etching characteristics of PbS.

N. Menyuk
A. S. Pine

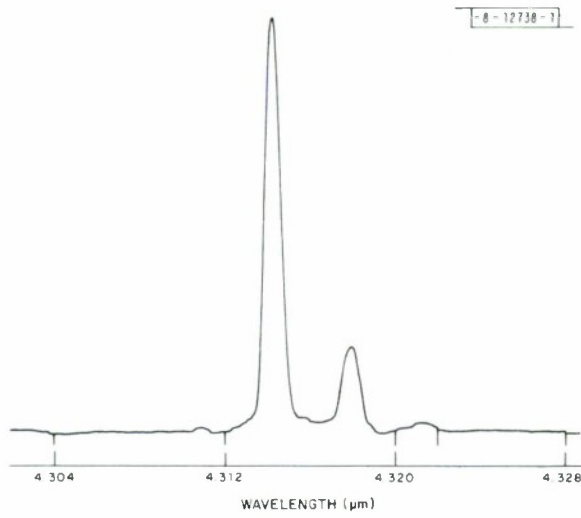
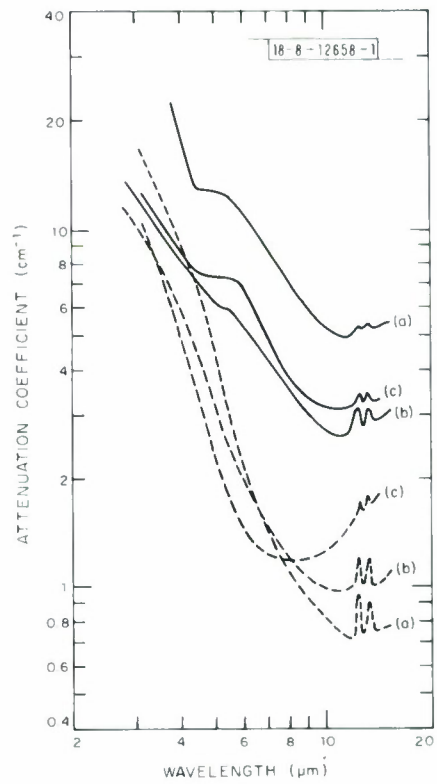


Fig. II-7. Spectrum of vapor-grown PbS laser transverse-pumped with GaAs diode laser.

Fig. II-8. Attenuation coefficient for CdGeAs₂ at room temperature (solid curve) and at liquid nitrogen temperature (dashed curve) for (a) as-grown sample, (b) Li annealing for 3 days, and (c) Li annealing for 10 days.



B. INFRARED NONLINEAR MATERIALS

1. Infrared Transmission of Li-Diffused CdGeAs₂ Samples

We have found that the infrared transmission for as-grown CdGeAs₂ samples can be improved by annealing in a Li atmosphere for several days at a temperature of 630°C, which is approximately 30°C below the melting point of CdGeAs₂. Figure II-8 shows the attenuation coefficients as a function of wavelength measured at room temperature and liquid nitrogen temperature for a CdGeAs₂ sample, first as-grown and then after Li diffusion for 3 and 10 days. As seen, the room-temperature attenuation coefficients are reduced by the annealing process. However, the improvement is smaller than obtained by cooling an as-grown sample to liquid nitrogen temperature.

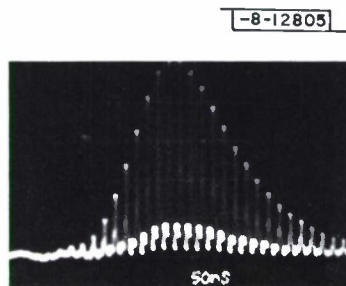
The attenuation at the shorter wavelengths was initially thought to be due to scattering, similar to what is observed for AgGaSe₂. However, using an integrating sphere, we have verified that there is no significant scattering at short wavelengths, and the remaining transmission losses at liquid nitrogen temperature must therefore be due to absorption. Most likely the absorption is associated with the deep acceptor levels (created by stoichiometric defects or impurities) that have been observed in both photoconductivity and Hall measurements.^{5,6}

The attenuation at short wavelengths varies from sample to sample, and experiments presently are being carried out to determine if there is a correlation between composition, electrical properties, and optical transmission.

2. SHG Efficiency in CdGeAs₂ at Liquid Nitrogen Temperature

We have measured the second-harmonic conversion efficiency for several CdGeAs₂ crystals at liquid nitrogen temperature using a CO₂ TEA laser operating in a TEM₀₀ mode with a pulse length of 150 nsec. The laser was spontaneously mode-locked with a pulse shape as shown in Fig. II-9. The highest external energy conversion of 12.8 percent was obtained for a 12.1-mm-long uncoated crystal with 3.9 J/cm² incident on the crystal. Correcting for reflection losses,

Fig. II-9. CO₂ TEA laser pulse shape.



this gives an internal conversion of 27.6 percent. For the above measurement, the spot size at the crystal was 250 μm. Cooling the crystals to liquid nitrogen temperature allows use of larger cross sections for second-harmonic generation because of improved uniformity in optical transmission, and for the 12.1-mm-long crystal the second-harmonic conversion efficiency was completely uniform over the entire cross section of 7 × 13 mm². To obtain more second-harmonic power, we changed the spot size at the crystal to 2.9 mm and increased the incident laser energy by adding nitrogen to the discharge and opening up the mode-limiting aperture inside the laser cavity. For an energy density of 2.4 J/cm² incident on the crystal,

-8-12806

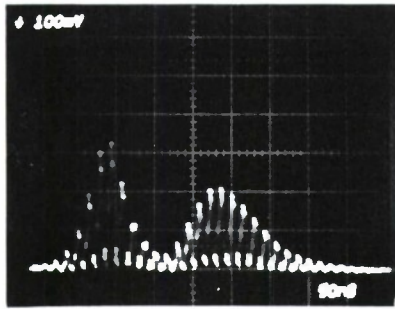


Fig. II-10. Second-harmonic pulse shape showing saturation.

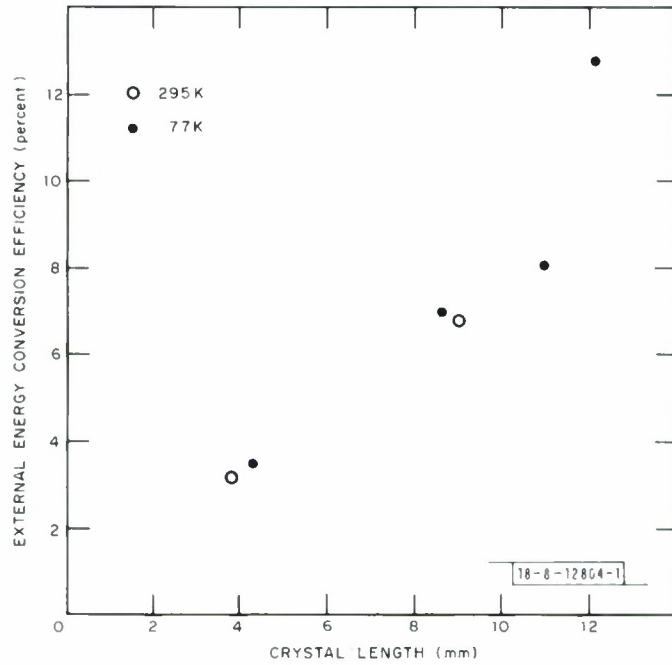


Fig. II-11. Maximum external energy conversion vs crystal length for second-harmonic generation in CdGeAs₂.

the second-harmonic energy obtained was 26 mJ and the external energy conversion efficiency was 8 percent. By filling the entire crystal, it should be possible to obtain up to 100 mJ of second-harmonic energy. Presently, however, we are limited by the TEM₀₀ mode output energy available from our TEA laser.

The saturation effects reducing the second-harmonic conversion efficiencies in room-temperature CdGeAs₂ samples⁷ also are present at liquid nitrogen temperature. Maximum conversion efficiency is usually obtained at an energy density slightly below the surface damage threshold for the crystals. Figure II-10 illustrates the saturation of the second-harmonic output pulse. It shows the pulse shape after an aperture that selected the center portion of the second-harmonic output beam for an incident CO₂ laser pulse shape as shown in Fig. II-9, and an energy density of 5.3 J/cm² which is close to the damage threshold.

Figure II-11 shows the maximum external energy conversion efficiency obtained by second-harmonic generation in CdGeAs₂ crystals cut from different boules. Most of the crystals had to be cooled to liquid nitrogen temperature to be useful. The conversion efficiency is found to increase approximately linearly with crystal length.

3. Surface Damage Threshold for CdGeAs₂, AgGaSe₂, AgGaS₂, Tl₃AsSe₃, and Ge

We have measured the optical surface damage threshold for CdGeAs₂, AgGaSe₂, AgGaS₂, Tl₃AsSe₃, and Ge at 10.6 μm using a spontaneously mode-locked CO₂ TEA laser operating in a TEM₀₀ mode with a pulse length of 150 nsec. Figure II-9 shows the laser pulse. The principal purpose of the measurements was to generate practical damage numbers for device design rather than to study the exact nature of the damage mechanisms, and we therefore used a fairly large spot size of 250 μm for most of the measurements. The most extensive studies were carried out on CdGeAs₂. We wanted to determine how polishing techniques, etching, vacuum, and cooling to reduce bulk absorption affected the damage threshold for this material.

The samples, 1 to 3 mm thick, were wedged to avoid interference effects. They were placed at the focal point of the laser beam, and the incident laser energy was adjusted using CaF₂ and polyethylene attenuators. The focused spot sizes were determined by measuring the transmission through several calibrated apertures. Before the damage measurements, the samples were cleaned using trichloroethylene and acetone.

For the initial measurements on CdGeAs₂, the damage threshold was defined by the formation of a visible plasma observed in a darkened room. Measurements were taken for three different spot sizes of 78, 250, and 412 μm, and it was found that the damage threshold which was about 10 J/cm² for the best samples was approximately independent of the spot sizes. (The beam area is defined as $\pi w^2/2$, where w is the spot size.) The experiment was then changed to include a 40X microscope, allowing us to observe changes on the surface in real time when the laser pulses were incident on the sample. We found that samples damage at lower power levels than the plasma damage threshold. For CdGeAs₂, the preplasma damage threshold, defined as the energy density where irreversible changes occur on the surface, was approximately a factor-of-two smaller. The damage starts with the formation of a few small pits much smaller than the laser spot size. They are generally less than 10 μm in diameter and randomly

TABLE II-1 RELATIVE DAMAGE THRESHOLDS FOR CdGeAs ₂			
Sample Conditions		Damage Threshold	
Temperature (K)	Surroundings	Pit Formation	Plasma Formation
298	Air	0.6	1.0
298	Vacuum	0.6	0.9
77	Vacuum	0.6	0.8

TABLE II-2 LASER DAMAGE THRESHOLDS MEASURED USING A TEM _{aa} MODE TEA CO ₂ LASER WITH A PULSE LENGTH OF 150 nsec AND FOCUSED TO A SPOT SIZE OF 250 μm		
Material	Damage Threshold	
	Pit Formation (J/cm ²)	Plasma Formation (J/cm ²)
CdGeAs ₂	5 to 6	9 to 10
AgGaSe ₂	1.5 to 3	4 to 5
AgGaS ₂	3 to 3.5	3.5 to 4
Tl ₃ AsSe ₃	1.5 to 2.5	3 to 5
Ge, single crystal, 57 Ω cm	5 to 6	19 to 20
Ge, polycrystalline	4	10

distributed. The number of pits increases with increasing incident laser energy. There is no clear correlation between where the pits are formed and surface scratches, although the pits are somewhat more concentrated along the scratches. The pit formation is probably due to heating of isolated micron- or submicron-sized inclusions near the surface and not due to absorption by a surface layer or electron avalanche. If damage occurs, it always starts with the first laser pulse. With several incident pulses slightly above the preplasma damage threshold, only the first few pulses give rise to pit formation. For succeeding pulses, nothing happens. At higher energies near the plasma damage threshold, the pit formation continues until the surface finally explodes and a strong visible plasma is observed. This produces a spherical central region looking like a molten crater. The difference in plasma damage threshold between 1 and 100 pulses incident on the samples appears to be small.

We have never observed bulk damage in room-temperature CdGeAs₂ samples. After repolishing the samples, no effect of damage can be observed. For example, damaged second-harmonic crystals are used over and over again after repolishing.

We have tried different polishing techniques for CdGeAs₂. No significant difference in damage threshold was found between mechanically and chemically polished samples. For the mechanical polishing, the last polishing step was with 1/4- or 1- μ m diamond paste. A 10-percent Br₂ solution was used for the chemical polishing. We have also subjected CdGeAs₂ to a mild etch of 1H₂O₂:2NH₄OH:4H₂O, and then immediately afterward measured the damage threshold. For a sample which had a damage threshold before etching comparable to the best we have measured for CdGeAs₂, there was no significant improvement. For another sample, however, which before etching had a damage threshold about a factor-of-two lower than for the best samples, there was improvement such that after etching the damage threshold was comparable to the best samples.

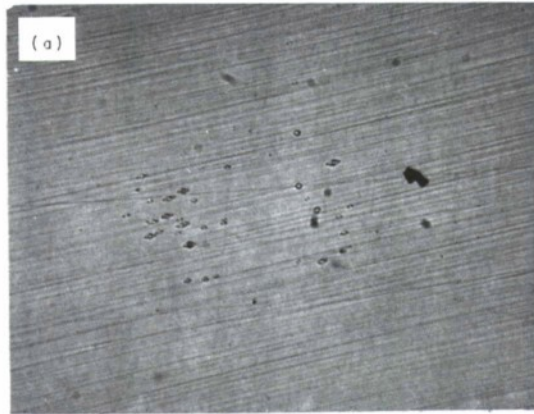
Recently, most of our second-harmonic experiments have been performed at liquid nitrogen temperature, and it is therefore of interest to measure the damage threshold at this temperature. Table II-1 shows the relative changes in the damage threshold for a sample mounted in air and under vacuum at room temperature and at liquid nitrogen temperature. As seen, the variations are small, indicating that the damage threshold is uncorrelated with the bulk absorption losses which are much smaller at liquid nitrogen temperature.

Table II-2 lists the measured damage thresholds for CdGeAs₂, AgGaSe₂, AgGaS₂, Tl₃AsSe₃, and Ge. The numbers are an average for the best samples we have measured. Of the nonlinear materials, CdGeAs₂ has the highest damage threshold, and it is almost as high as for Ge.

Figures II-12, II-13, and II-14 show the damage morphology for mechanically polished samples of CdGeAs₂, AgGaSe₂, and Ge after a single incident laser pulse. Etched samples of CdGeAs₂ generally show fewer pits than mechanically polished samples, although the damage thresholds are the same.

In the future, we are planning to study the damage threshold for CdGeAs₂ for longer pulse lengths and with and without mode-locking.

H. Kildal
G. W. Iseler



-8-12807-1

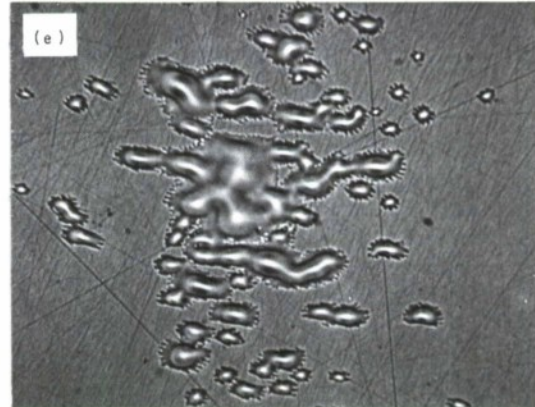
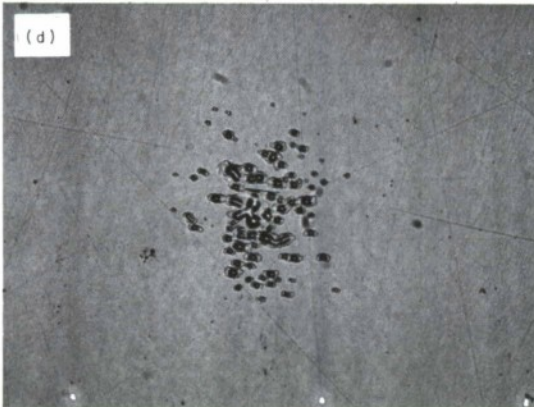
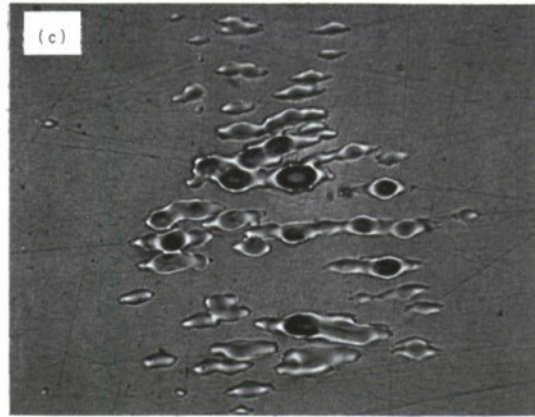
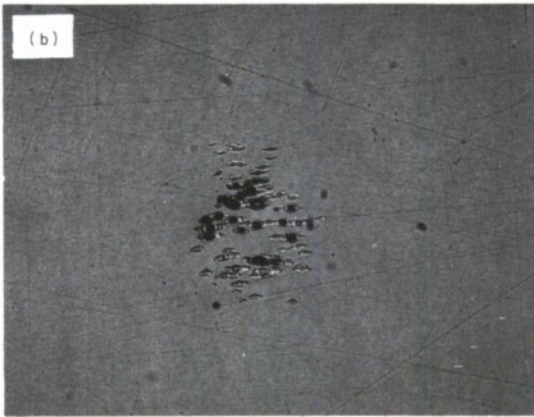


Fig. II-12. Damage morphology for single crystal of CdGeAs₂ at: (a) 5.7 J/cm² (160X, front surface); (b) 10.5 J/cm² (128X, front surface); (c) 10.5 J/cm² (320X, front surface); (d) 10.5 J/cm² (128X, back surface); (e) 10.5 J/cm² (320X, back surface).

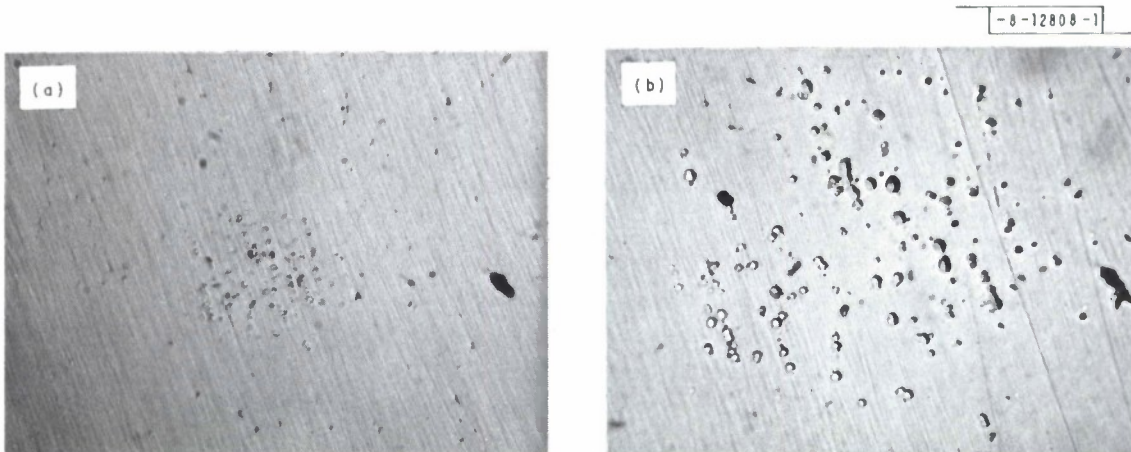


Fig. II-13. Damage morphology at back surface of single crystal of AgGaSe₂ at 3.3 J/cm²: (a) 160X, and (b) 320X.

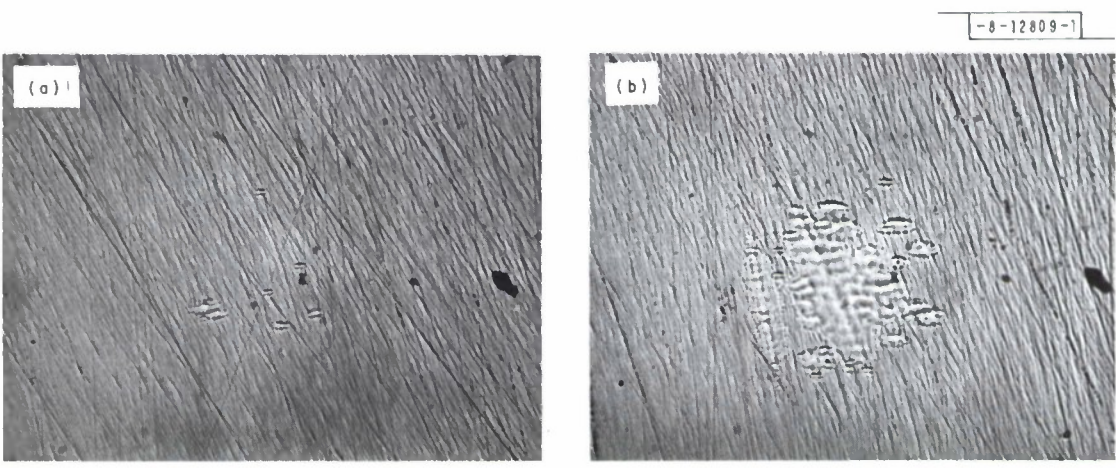


Fig. II-14. Damage morphology at front surface of polycrystalline Ge at (a) 9.6 J/cm², (b) 13.4 J/cm², with 160X magnification.

C. ELECTRO-OPTIC MODULATOR FOR SUBMILLIMETER RADIATION

Two types of modulators have been applied successfully to submillimeter radiation. The first⁸ depends on the absorption of impact-ionized free carriers in Ge, while the second⁹ is an extension of microwave ferrite devices and uses the Faraday effect. These modulators lack the high-frequency response and phase control typically available from electro-optic¹⁰ devices currently used at infrared and visible wavelengths.

We report the first electro-optic modulator developed for the submillimeter. Since the half-wave voltage of an electro-optic modulator is proportional to λ/n^3r (n is the index of refraction, and r is the electro-optic coefficient), one may expect them to be inefficient in the long-wavelength regime. However, in the submillimeter below the lattice optical-mode frequencies, n and r are increased¹¹ due to an ionic (lattice) contribution to the polarization.

For our device, we selected a LiTaO_3 crystal cut and polished to dimensions $0.5 \times 0.5 \times 1.0 \text{ cm}^3$ with electrodes plated on the two a, b crystallographic faces parallel to the optical propagation. The absorption losses anticipated in this wavelength region are largely a consequence of one- and two-phonon processes involving optical phonon modes. These are significantly reduced by cooling to He temperatures where a transmission of 27 percent was determined for our sample. The absorption clearly is quite small, since reflection at each interface is estimated to be about 45 percent. Figure II-15 is a schematic representation of the modulator.

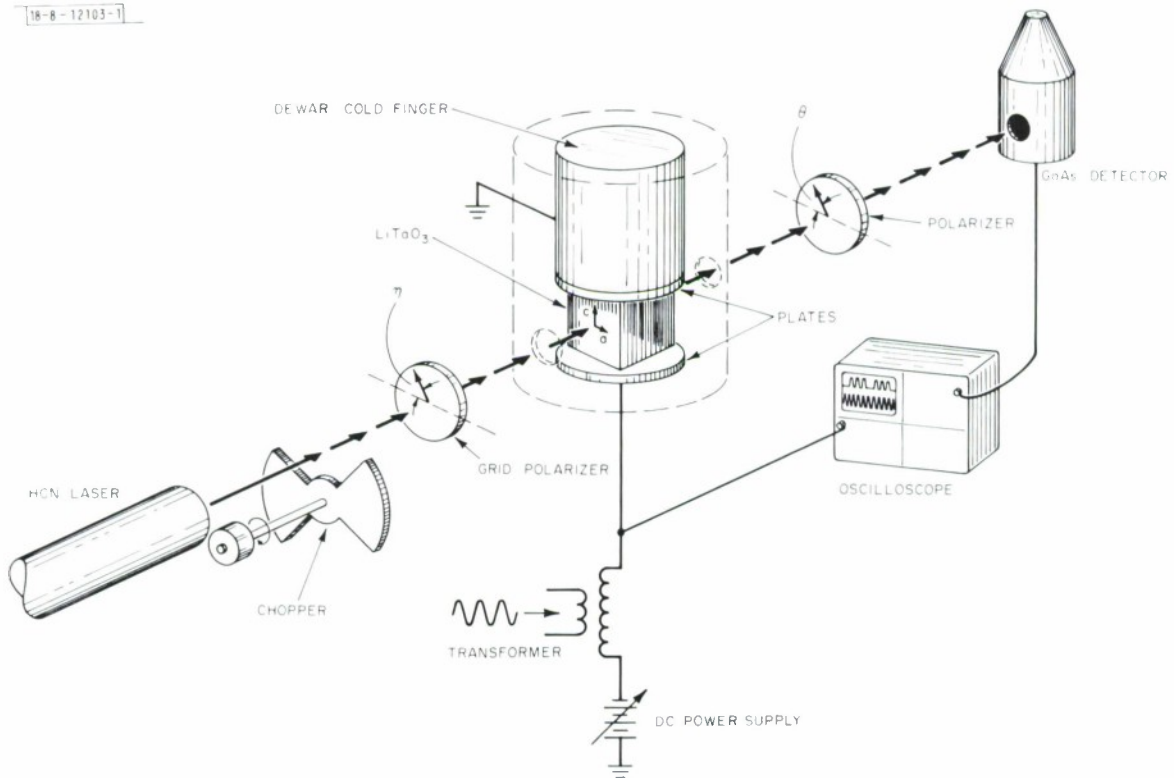


Fig. II-15. Experimental configuration of submillimeter electro-optic modulator. Polarizers are made from gold grid (1000 L.P.I.) deposited on mylar. Crystal belongs to $3m$ crystallographic point group and has largest electro-optic effect when voltage is applied along c -axis (electrodes on a, b faces) and light propagates perpendicular to c -axis.

Figure II-16 shows the output of an HCN laser mechanically chopped while a simultaneous sinusoidal modulation voltage at 600 Hz was applied to the crystal. The depth of modulation was greater than 90 percent with 10 kV applied as shown in the lower trace. Using the values for the indexes of refraction extrapolated from the data of Barker,¹² we determine a value for $r_{33} = -2.8 \times 10^{-11}$ m/V in comparison with theoretical predictions of -3.3×10^{-11} m/V (Ref. 11). Because of the high index of refraction at these long wavelengths, modulation also results from the Fabry-Perot interferometer formed by the parallel LiTaO₃ crystal faces. This effect¹³ has been observed and can probably be eliminated by suitable surface treatment or antireflection coatings.

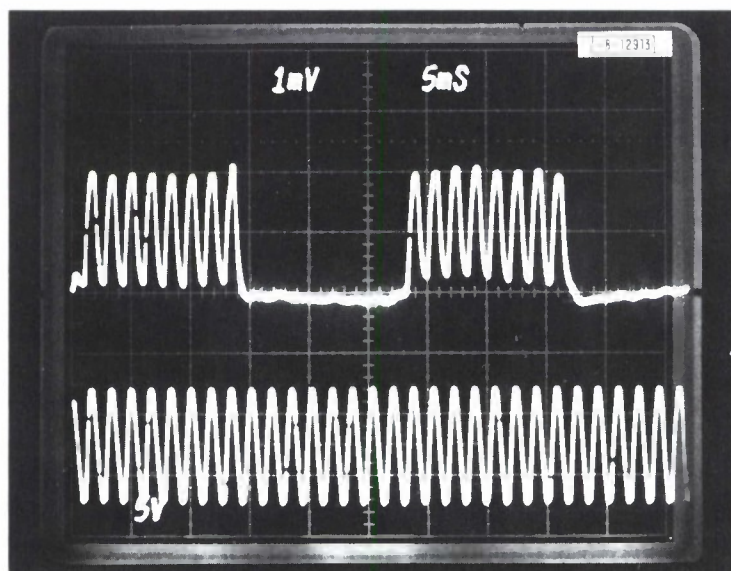


Fig. II-16. Upper trace is 337- μ m laser radiation mechanically chopped, along with simultaneous 600-Hz modulation by electro-optic crystal. Lower trace is applied voltage on crystal measured with 1:1000 divider.

The modulator has been tested up to 125 kHz with harmonics detected at 250 kHz. At present, we see no fundamental limitation for this modulator up to gigahertz frequencies. Our initial results indicate that this type of electro-optic crystal may be useful¹⁴ for both frequency modulation and beam control of submillimeter laser beams.

H. R. Fetterman W. E. Barch
Chenming Hu[†] C. D. Parker

[†] Department of Electrical Engineering, M.I.T.

REFERENCES

1. A. S. Pine and N. Menyuk, *Appl. Phys. Lett.* 26, 231 (1975).
2. E. D. Hinkley and R. T. Ku, "Diode Laser Multi-Pollutant Ambient Air Monitoring," Annual Report to NSF and EPA, Lincoln Laboratory, M.I.T. (June 1974).
3. R. S. Eng, P. L. Kelley, A. Mooradian, A. R. Calawa, and T. C. Harman, *Chem. Phys. Letters* 19, 524 (1973), DDC AD-771905/7.
4. A. Mooradian, A. J. Strauss, and J. A. Rossi, *IEEE J. Quantum Electron.* QE-9, 347 (1973), DDC AD-759091.
5. I. P. Akimchenko, A. S. Borshchevskii, and V. S. Ivanov, *Sov. Phys.-Semicond.* 7, 98 (1973).
6. H. Kildal, "CdGeAs₂ and CdGeP₂ Chalcopyrite Materials for Infrared Nonlinear Optics," Stanford University, Air Force Materials Laboratory Technical Report AFML-TR-72-277, Air Force Systems Command, Wright-Patterson Air Force Base, Ohio (December 1972).
7. H. Kildal and J. C. Mikkelsen, *Opt. Commun.* 10, 306 (1974), DDC AD-A000516/5.
8. I. Melngailis and P. E. Tannenwald, *Proc. IEEE (Letters)* 57, 806 (1969), DDC AD-693896.
9. J. Bireh and R. G. Jones, *Infrared Phys.* 10, 217 (1970).
10. R. T. Denton, F. Chen, and A. A. Ballman, *J. Appl. Phys.* 38, 1611 (1967).
11. G. D. Boyd, T. Bridges, M. Pollack, and E. Tuner, *Phys. Rev. Lett.* 26, 387 (1971).
12. A. S. Barker, Jr. and A. A. Ballman, *Phys. Rev. B* 2, 4233 (1970).
13. E. I. Gordon and J. D. Rigden, *Bell Syst. Tech. J.* 42, 155 (1963).
14. V. J. Corcoran, *IEEE Trans. Microwave Theory Tech.* MTT-12, 1103 (1974).

A. CRYSTALLIZATION OF AMORPHOUS SILICON FILMS
BY Nd:YAG LASER HEATING

Single-crystal Si solar cells have been the most successful photovoltaic devices in achieving good efficiency and reliability, but their present cost makes their use prohibitively expensive for large-scale terrestrial applications. The cost of solar cells could be reduced greatly by the development of procedures for preparing large-grain, thin-film Si material that would be adaptable readily to mass-production device-fabrication methods. In this connection, we have recently succeeded in converting sputtered, amorphous Si films to crystalline Si by heating with a focused Nd:YAG laser.

If a high-power laser beam is focused on the surface of a Si film that absorbs at the laser frequency, the film can be heated locally to a temperature¹ high enough to cause crystallization. With an unseamed Ar-ion laser beam focused to a circular image, thin polycrystalline Si films of 1- μm thickness, with grains smaller than 0.1- μm diameter, have been recrystallized to grains as large as 5 μm (Ref.2). However, the Ar-ion laser is very inefficient (overall power efficiency of about 0.05 percent). In addition, because of the high absorption coefficient of Si at the frequencies of the Ar-ion laser, heating is limited to the surface layer, probably making this laser unsuitable for preparing Si films of sufficient thickness ($\geq 10 \mu\text{m}$) for solar cells.

In our studies, we have concentrated on the use of the Nd:YAG laser (overall power efficiency ~ 2 percent). The laser wavelength is 1.06 μm (1.17 eV), which is just within the absorption edge of crystalline Si. The absorption coefficient α of crystalline Si at this wavelength is about 20 cm^{-1} (Ref.3), and hence only a few percent of the laser power will be absorbed by a film 10 μm thick.

Amorphous Si has a much broader absorption edge than crystalline Si, with band tailing states that narrow the effective band gap. At 1.06 μm , for an 11- μm -thick, amorphous Si film, the measured transmission is less than 0.1 percent. Thus, initially amorphous Si films strongly absorb the Nd:YAG laser power, and such films can be heated easily to a temperature where crystallization occurs [$\sim 700^\circ\text{C}$ (Ref.1)]. Although the band gap tends to increase as the Si crystallizes, this tendency can be compensated by a number of effects, among them the thermal narrowing of the band gap of crystalline Si,

$$\frac{dE_g}{dT} \cong -3 \times 10^{-4} \text{ eV/K}$$

where E_g is the band gap, and T is the absolute temperature.⁴ One might therefore expect the physical characteristics of an amorphous Si film to change in a complex manner as the incident laser power is increased sufficiently to cause crystallization. We have indeed observed such behavior in optical transmission during the laser crystallization of amorphous films.

Several Si films ranging from 6 to 11 μm in thickness were deposited on 25-mm-diameter, single-crystal Al_2O_3 substrates [(0001) face] by RF sputtering. The substrate temperature during deposition was estimated to be 200 $^\circ\text{C}$. The films were found to be amorphous by both x-ray diffraction and reflection electron microscopy.

The samples were mounted on a water-cooled copper block in a cylindrical Pyrex experimental chamber containing an 85% Ar-15% H_2 atmosphere. The Nd:YAG laser is a multimode

unit, pumped by a tungsten lamp, with maximum CW power output of 7 W. The laser beam was focused on the film by a 25-mm-focal-length quartz lens. The spot size varied somewhat, depending on focusing conditions, but was typically about 50 μm wide and 100 μm long. The copper block was inclined at 45° to the beam in order to allow monitoring the film appearance and spot color as a function of laser power.

Figure III-1 shows the laser power transmitted through an 8- μm -thick, amorphous Si film as a function of incident laser power. (The copper mounting block had a 6-mm-diameter hole for *in situ* transmission measurements.) As the incident power was first increased from zero, the transmitted power increased until the incident power reached about 1.5 W. At this point, the film appeared dull red in the region of the laser-beam focus. Further increase in incident power actually decreased the amount of transmitted power. At about 6 W of incident power, the spot at which the laser beam impinged appeared white-hot (in fact, in another experiment film evaporation occurred at an incident power of 7 W). The laser power was then decreased. For a given incident power, the transmitted power was much larger during the cooling half of the cycle than during the heating half. When the cycle was repeated, it was found that transmitted-vs-input-power curves for both the heating and cooling half-cycles were essentially the same as the curve for the cooling half of the first cycle. (A complete heating and cooling cycle took approximately

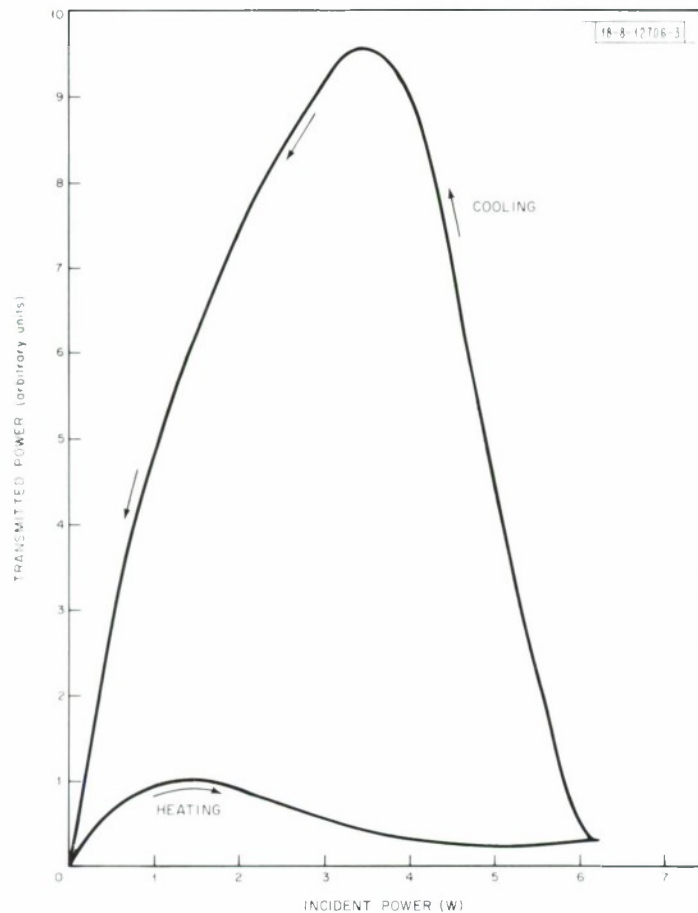


Fig. III-1. Plot of power transmitted through initially amorphous Si film 8 μm thick vs incident laser power, for first heating and cooling cycle.

10 minutes.) The experiment was repeated many times at different spots on this film as well as on several other initially amorphous films, and similar results were obtained.

These results indicate that irreversible structural changes occur in amorphous Si films at high enough incident laser power. We believe that the maxima in both the heating and cooling curves of Fig. III-1 are due in part to the decrease in band gap with temperature, although additional, nonlinear processes are probably involved.

In order to prepare an area of crystallized material large enough for further characterization, the film was scanned laterally (using 6 W laser power) at the rate of ~ 1.2 cm/min. with successive overlapping scan lines centered $25 \mu\text{m}$ apart. The scan rate was limited by the mechanical drive system available and not by sample-heating requirements. Areas of about 0.5×0.25 cm were readily scanned.

To examine the structure of the Si films, reflection-electron-diffraction pictures were taken in a JEM-120 electron microscope at 80-keV electron energy. Figure III-2(a) is the diffraction pattern of an amorphous, $8\text{-}\mu\text{m}$ -thick film before laser heating, while Fig. III-2(b) is the pattern obtained for a laser-heated area of the same film. The diffraction spots in the latter pattern show that this area is quite ordered. The faint rings in this pattern, which have been identified as due to Si diffraction, indicate the presence of a small amount of fine-grained material. The electron-beam spot size at the sample is larger than $2 \mu\text{m}$. In the reflection-diffraction mode of operation, the electron beam is incident at a very small grazing angle ($\sim 1^\circ$) with respect to the sample. Therefore, the exact area intercepted is not known, but is much greater than $(2 \mu\text{m})^2$. Linear motion of the microscope stage by about $25 \mu\text{m}$ in the laser-heated area did not significantly alter the spot patterns, indicating crystallite sizes of at least $25 \mu\text{m}$. (Other parts of the treated film showed similar patterns, but some regions were not as crystalline.) Similar results were obtained for other films.

X-ray diffraction patterns for films that had been treated showed sharp Si lines. For some of the films, the lines were so sharp that their width could be attributed to instrumental broadening alone. However, since the x-rays sampled a large area (estimated to be about 1×5 mm), several Si lines were always present.

Laser-heated films have been examined by optical microscopy, but the results are inconclusive. The films show scanning tracks with discrete features of dimensions up to $\sim 25 \mu\text{m}$. On surfaces lapped with Syton and a few volume percent of H_2O_2 ,[†] these features become more pronounced, but cannot be definitely identified as crystallites. Preliminary scanning-electron-microscope inspection of treated films in cross section shows them to be dense and featureless.

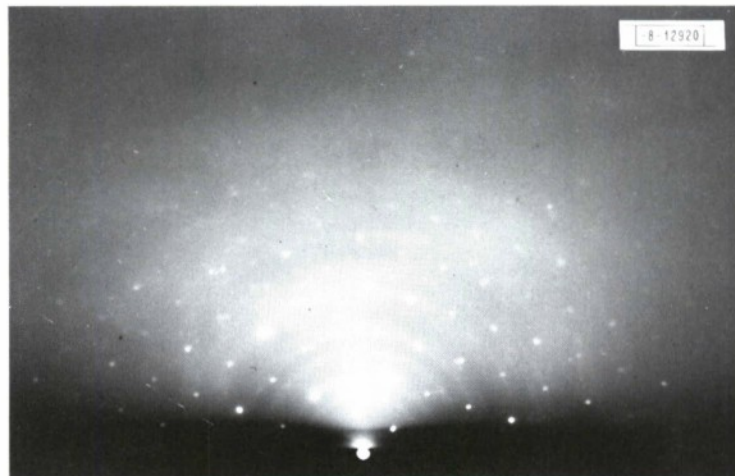
Although the above experiments were performed on amorphous Si films on single-crystal Al_2O_3 substrates, similar results can be expected for films deposited on other substrates with thermal properties close to those of Al_2O_3 . Preliminary crystallization experiments, performed on an $11\text{-}\mu\text{m}$ -thick film sputtered on a fused-silica substrate, yielded x-ray-diffraction and reflection-electron-microscopy patterns resembling those described above.

J. C. C. Fan P. M. Zavracky
H. J. Zeiger M. C. Finn

[†] This process is known to bring out grain structures for Si surfaces. We wish to thank M. C. Cretella for suggesting this process.



(a)



(b)

Fig.III-2. Reflection electron microscope pictures of Si film: (a) amorphous, untreated film; (b) same film after treatment with Nd:YAG laser radiation.

B. MEASUREMENT OF IONIC CONDUCTIVITY IN SOLID ELECTROLYTES

Ceramic membranes capable of fast Na^+ -ion transport at 300°C are needed for the Na-S secondary battery, which promises specific energies of 100 Wh/lb at power densities of 100 W/lb. Although membranes of β - and β'' -alumina have sufficiently high Na^+ conductivity, they tend to develop short circuits on repeated recharging if a critical charging voltage is exceeded. Since this undesirable characteristic may arise from the layer structure of these aluminas, we are investigating Na^+ -ion transport in cubic skeleton structures, which have three-dimensional tunnel arrays.⁵ We find, for example, that 95-percent dense disks of $\text{NaSbO}_3 \cdot 1/6\text{NaF}$ have approximately half the conductivity at 300°C and twice the activation energy for Na^+ -ion mobility of β -alumina. However, we need a better understanding of the ion-transport mechanism and of the structure-related factors which influence it. To this end, we have investigated ionic conductivity in greater detail by measuring (for the first time) the transient current response of solid electrolytes to constant-voltage pulse trains.

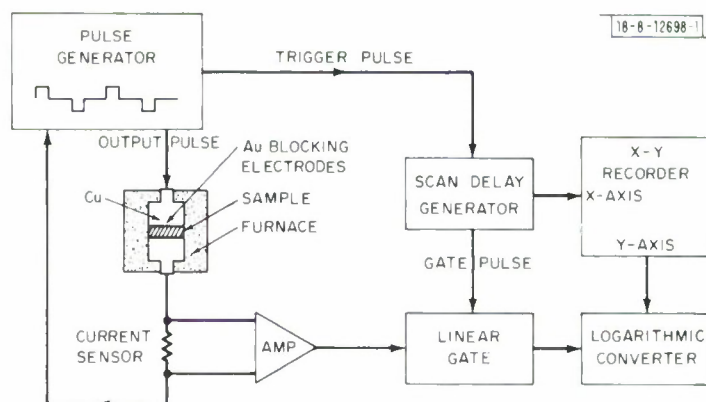


Fig. III-3. Diagram of experimental arrangement for measuring transient current response of sample with blocking electrodes to train of constant-voltage pulses.

Figure III-3 shows the experimental arrangement. The sample is placed between two copper electrodes, but separated from them by thin sheets of gold that serve as blocking electrodes. The initial measurements, which employed gold sheets only $2.5\ \mu\text{m}$ thick, were plagued by a lack of reproducibility resulting primarily from diffusion of copper through the gold and into the samples. The quality of the data has been improved greatly by the use of self-aligning copper electrodes together with $250\text{-}\mu\text{m}$ gold sheets for blocking. Pulse trains, consisting of constant-voltage pulses of alternating polarity (to avoid permanent polarization of the sample) separated by quiescent intervals, are applied to the electrodes. The pulse risetime is approximately 100 nsec. The pulse amplitude can be varied from 0.1 to 10 V, the width from 1 msec to 5000 sec, and the duty cycle from 12 to 100 percent. The current that flows in the external circuit is first preamplified, then sampled by a gated amplifier, compressed by a logarithmic converter, and finally plotted as a function of time on an X-Y recorder.

The simplest equivalent circuit for a ceramic electrolyte with reversible electrodes consists of an interior resistance R in series with the parallel combination of a capacitance C_b and resistance R_b arising from the grain boundaries (see Fig. III-4). This model neglects parallel paths

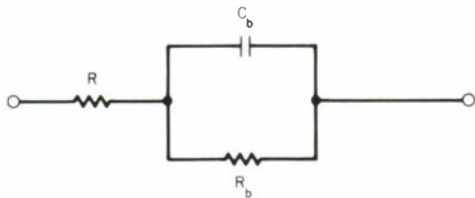


Fig. III-4. Simplest equivalent circuit for ceramic electrolyte with reversible electrodes.

through neighboring grains, which requires that the boundary impedance be high compared with the interior resistance. Recent measurements of impedance as a function of frequency by Powers and Mitoff⁶ show that this condition is satisfied for β -alumina. They find the transition region from the low-frequency impedance ($R + R_b$) to the high-frequency impedance R to be somewhat broader than calculated from the equivalent circuit, but give the plausible rationale that one should expect a distribution of grain-boundary impedances.

If blocking electrodes are used, the equivalent circuit includes an additional contact capacitance C in series with the internal resistance R . The current vs time response of such a circuit to charging by an applied voltage step consists of two regions of exponential decay separated by a brief transition interval. Thus, the graph of $\log I$ vs t would consist of two straight lines and a curved transition region that appears brief indeed on a time scale that extends over six orders of magnitude from 100 nsec to 100 msec. The decay of its current response to a voltage pulse is a more distinctive characteristic of the circuit than the frequency dependence of its impedance.

In contrast to this theoretical behavior, all our measurements on hot-pressed polycrystalline samples of various materials (e.g., $\text{NaSbO}_3 \cdot 1/6\text{NaF}$, $\text{NaTa}_2\text{O}_5\text{F}$, β -alumina) show a smooth, sweeping curvature in graphs of $\log I$ vs t from 100 nsec to 100 sec. An explanation of this shape in terms of a reasonable distribution of grain-boundary impedances is not plausible, and we therefore have been forced to re-examine the basic mechanisms of ionic conduction in these materials.

Let $p(x, t)$ denote the concentration of mobile charge, $i(x, t)$ the current density, and $E(x, t)$ the electric field. Then, the distribution of ions inside a continuous medium is to be found by solving the differential equation:

$$\frac{\partial}{\partial t} p(x, t) = -\frac{\partial}{\partial x} i(x, t) = -\frac{\partial}{\partial x} [\mu(x) p(x, t) E(x, t) - D(x) \frac{\partial}{\partial x} p(x, t)] \quad (\text{III-1})$$

where $\mu(x)$ and $D(x)$ are the mobility and diffusion constant, respectively. A grain boundary is a narrow region in which the mobility μ_b differs from μ in the bulk material. In fast-ion conductors, μ_b is much smaller than μ so that a surplus of carriers piles up on one side of the boundary region, while a deficiency arises on the other. Thus, a large concentration gradient is established across a grain boundary. Equilibrium is not attained until the carriers find their way through the boundary region. Since the diffusion term is non-ohmic, no equivalent circuit can be a valid representation of Eq. (III-1) unless $D(\partial p/\partial x)$ is negligible for all x and all t .

In our most recent pulse experiments, in addition to measuring the decay of the charging current we also have measured the decay of the discharge current that flows during the quiescent intervals between pulses. The two decays must be identical for any ohmic equivalent circuit (unless electronic current shunts the contact capacitance, in which case the total amounts of

transported charge will differ). We find a difference in the decay curves, but with the same total charge transferred during discharge as during the charging cycle, which indicates the presence of a diffusion current. The discharge current is greater than the charging current initially, but then decays faster, in agreement with the predicted behavior of a diffusion contribution from the bulk. Conventional AC techniques would have been unable to demonstrate this presence of a diffusion contribution to the current.

Since the mobility is lower at grain boundaries, we can expect the diffusion term to be even more important there than in the bulk. We conclude that the observed curvature in the relation $\log I$ vs t is in large part due to the discharge of C_b by a predominantly diffusive current. Thus, comparison between experiment and solutions of Eq. (III-1) should yield important insight into the character of grain boundaries in ceramic electrolytes.

K. Dwight
J. A. Kafalas
H. Y-P. Hong

C. SURFACE LOSS FUNCTIONS OF TITANIUM AND VANADIUM OXIDES DERIVED FROM OPTICAL DATA

Transition-metal oxides, particularly TiO_2 , are currently of interest as catalytic electrodes in the photoelectrolytic decomposition of water into H_2 and O_2 by sunlight.^{7,†} It has been conjectured[†] that surface states near the middle of the forbidden gap in n-type TiO_2 may be important in this process; and recent electron-energy-loss (ELS) experiments⁸ on atomically clean crystals of both TiO_2 and Ti_2O_3 , which were subsequently oxidized or reduced by sputter-etching them with either Ar or O_2 ions, have confirmed the existence of such surface states in TiO_2 . We now provide further confirmation of this result by comparing the observed ELS spectrum of the respective materials with the surface loss function $\text{Im}[-1/(\epsilon + 1)]$ calculated from the bulk dielectric function $\epsilon(\omega)$ determined from optical data.⁹ We also have used the available optical data¹⁰ to obtain the surface loss function for a pure Ti crystal for comparison and also for V, V_2O_3 , and VO_2 .

As is well known, ELS is the electronic analog of Raman scattering spectroscopy: an electron incident on a solid surface excites some electronic transition and is then emitted with a corresponding lower energy. Consequently, ELS provides information about interband and excitonic transitions, plasma oscillations, and (at sufficiently low primary beam energies ≤ 10 eV) surface states. As a technique for characterization of surface electronic states, ELS gives energy differences between features in the filled and empty density of states. The main feature of the experimental results reported in Ref. 8 is a strong loss peak at 4.5 eV that is present in the ELS spectra of Ti_2O_3 and reduced TiO_2 but not in the spectrum of a fresh surface of TiO_2 . The occurrence of this peak is evidently associated with the presence of Ti^{3+} ions, since only Ti^{4+} ions are present on a fresh surface of TiO_2 . As Ti^{3+} has one d-electron, the 4.5-eV peak presumably arises from the transition between d-levels split by the trigonal component of the crystalline field. The 4.5-eV peak and the additional peaks observed at 5.5, 10.0, and 13.5 eV are accounted for nicely by the transitions given by Goodenough's energy-level model in Fig. III-5, provided the peak at 13.6 is shifted to 14 eV. In view of the resolution of about 0.8 eV in the ELS measurement,⁸ such a shift is consistent with the uncertainty in the location of the peaks. All the peaks except at 4.5 eV also occur in the ELS spectrum of TiO_2 .

† See p. 32 in Ref. 5.

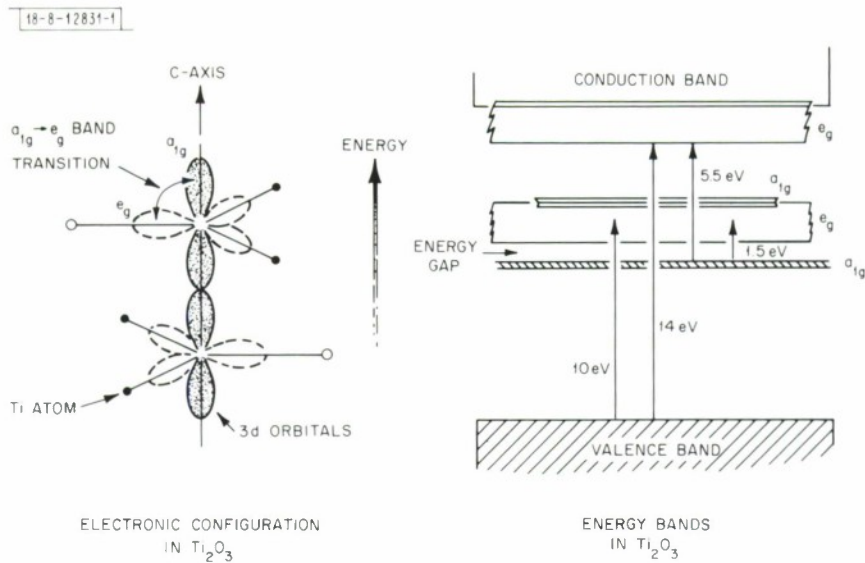


Fig. III-5. Electronic configuration and energy level model of Ti_2O_3 showing transitions associated with peaks in ELS spectrum of Ref. 8.

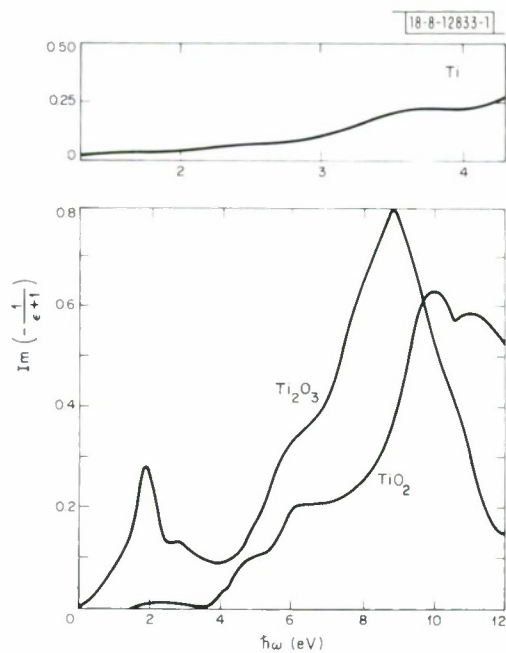


Fig. III-6. Surface loss function $Im \left[\frac{-1}{\epsilon + 1} \right]$ vs $\hbar\omega$, derived from optical data for pure Ti (Ref. 10), Ti_2O_3 , and TiO_2 (Ref. 9). Optical spectrum has been averaged over two polarizations (parallel and perpendicular to e-axis).

Turning now to the optical data,⁸⁻¹¹ we observe that the ELS spectrum is given formally¹² by the surface loss function $\text{Im}[-1/(\epsilon + 1)]$. We would expect, therefore, that unless the bulk states of an unreduced surface are totally different from the surface states, then the loss function with bulk dielectric function $\epsilon(\omega)$ will recapture most of the structure found from the ELS measurement.⁸ The loss functions derived in this way from optical data^{9,11} for Ti, Ti_2O_3 , and TiO_2 are shown in Fig. III-6, and those derived from optical data^{10,11} for V, V_2O_3 , and VO_2 are shown in Fig. III-7. In Fig. III-6, we observe a strong peak at 1.9 eV for Ti_2O_3 , which is clearly identifiable with the peak at 1.5 eV reported in Ref. 8 (within the limit of experimental error). The loss function derived from the optical data has an additional small peak at about 2.9 eV (which exists only for polarization parallel to the c-axis of the crystal⁹) and peaks near 5.8 and 9 eV which are identifiable with the 5.5- and 10.0-eV peaks of Ref. 8; and the loss functions for TiO_2 and for pure Ti do not exhibit 1.5-eV structure, as expected. In Fig. III-7, we observe a distinct loss peak at about 1.5 eV for VO_2 (which is to be expected from the fact that V^{4+} , like Ti^{3+} , has one 3d electron in a noncubic crystalline field). In V_2O_3 , it is not clear whether the loss peaks centered around 1.3 and 2.7 eV correspond to the doublet in the two-electron crystal-field-split optical spectrum of vanadium-doped Al_2O_3 . The loss spectrum for pure V is also shown in Fig. III-7 for comparison.

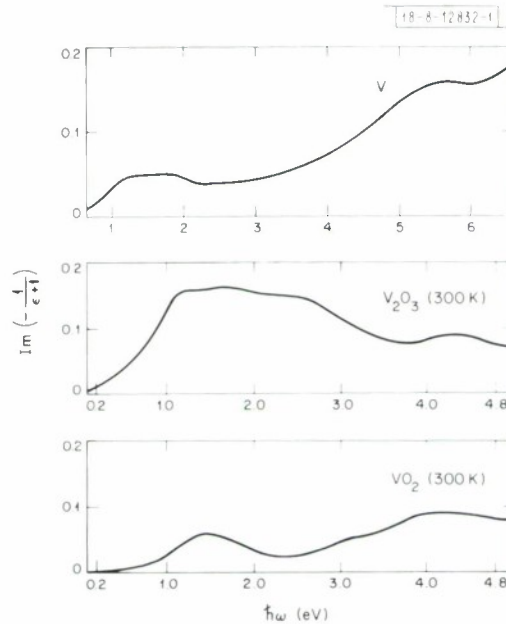


Fig. III-7. Surface loss function $\text{Im}[-1/(\epsilon + 1)]$ vs $\hbar\omega$, derived from optical data for pure V (Ref. 10), V_2O_3 , and VO_2 (Ref. 11).

From the agreement between the peak positions in the surface loss function of Fig. III-6 (determined from the bulk dielectric constant) and in the ELS spectra of Ref. 8, we can draw the obvious conclusion that the bulk dielectric function and the surface one are similar, at least for the titanium oxides. This implies that the bulk and surface d-band splittings are comparable in

these narrow-band materials. Formal analysis of the relationship between the loss function and the electronic energy bands in terms of the two-particle Green's function shows that this conclusion is probably true.

A.O.E. Animalu

D. ELECTRON MICROPROBE ANALYSIS OF $\text{Ga}_{1-x}\text{Al}_x\text{As}$ LAYERS

Electron microprobe analysis is widely utilized for determining the alloy composition of $\text{Ga}_{1-x}\text{Al}_x\text{As}$ layers, grown by liquid-phase epitaxy on GaAs substrates, that are incorporated into GaAs- $\text{Ga}_{1-x}\text{Al}_x\text{As}$ heterostructures used for light-emitting diodes, diode lasers, and other devices. We have obtained accurate analyses of such layers more than about 10 μm thick by a microprobe procedure that employs an electron acceleration voltage of 25 kV and standards of GaAs and elemental Al for determining the weight fractions of Ga and Al, respectively. When the measured weight fractions are converted to the mole fractions of GaAs ($1-x$) and AlAs (x), the total of x and $(1-x)$ normally differs from the expected value of 1 by no more than ± 0.03 .

For the analysis of $\text{Ga}_{1-x}\text{Al}_x\text{As}$ layers 5 μm thick or less, it is necessary to reduce the electron acceleration voltage below 25 kV in order to avoid excitation of Ga radiation from the GaAs substrate. In initial measurements on such thin layers, employing 15 kV acceleration, we found that the total of x and $(1-x)$ was consistently about 1.25, indicating a significant error in the analysis. The use of an elemental Al standard was suspected to be one source of error, both because inaccuracies are likely to result when the x-ray signal from pure Al is compared with the signal from Al in a matrix containing large proportions of other elements and also because x-ray absorption by the thin layer of Al_2O_3 always present on metallic Al tends to reduce the intensity of the signal from the standard. To avoid these difficulties, we have developed a procedure that uses a thick LPE layer of $\text{Ga}_{1-x}\text{Al}_x\text{As}$ as the standard for determining both Ga and Al in the thinner layers. This procedure has been found to give satisfactory accuracy for layers down to about 1 μm thick.

The LPE layer used as the standard is 23 μm thick, with a composition of $\text{Ga}_{0.358}\text{Al}_{0.642}\text{As}$. This composition was found by microprobe measurements at acceleration voltages of 15, 20 and 25 kV, in which a single-crystal wafer of GaAs was used as the standard for determining both Ga and As. There was no significant difference between the data taken at the different voltages. Table III-1 gives the Ga and As weight fractions obtained by averaging the results of independent determinations made at eight different locations on the layer surface. The maximum variation in these results is indicated by the limits of error given for each element. Table III-1 also gives the weight fraction of Al, which was determined by difference in order to avoid the use of an elemental Al standard.

In analyzing the thinner LPE layers, the electron acceleration voltage is reduced to 10 kV, which gives an estimated penetration depth of $\sim 1 \mu\text{m}$. X-ray intensity measurements are made for the Ga $L\alpha$ line and the Al $K\alpha$ line. Since the excitation energies for these lines are similar (1.11 and 1.56 keV, respectively), the sample volumes analyzed for the two elements are comparable. The raw intensity data are converted to chemical compositions by using the MAGIC IV computer program.¹³ Typical analyses obtained in this manner for five $\text{Ga}_{1-x}\text{Al}_x\text{As}$ layers ranging in thickness from 5.0 to 1.3 μm are given in Table III-2. Columns 2 and 3 list the measured mole fractions of GaAs and AlAs. Each of these values was found by averaging the results of independent determinations made at eight different locations on the layer surfaces. The fourth column gives the total of the two measured mole fractions. Note that the difference between

TABLE III-1 ANALYSIS OF STANDARD $\text{Go}_{1-x}\text{Al}_x\text{As}$ LAYER		
Element	Weight Fraction	Atom Fraction
Go	0.213 ± 0.006	0.358
As	0.639 ± 0.016	1.000
Al	0.148†	0.642

† Determined by difference.

TABLE III-2 ANALYSIS OF $\text{Go}_{1-x}\text{Al}_x\text{As}$ LAYERS					
Thickness (μm)	Mole Fraction			Normalized Mole Fraction	
	GoAs	AlAs	Total	GoAs	AlAs
5.0	0.976	0.026	1.002	0.974	0.026
5.1	0.481	0.538	1.019	0.472	0.528
3.2	0.857	0.146	1.003	0.854	0.146
2.7	0.344	0.661	1.005	0.343	0.657
1.3	0.930	0.126	1.056	0.881	0.119

this total and 1 is less than 0.02 for the first four layers, and that even for the thinnest layer this difference is only 0.056. The last two columns of the table give the reported mole fractions of GaAs and AlAs, which were normalized to give a total of 1.

M. C. Finn

REFERENCES

1. A. Lewis, Phys. Rev. Lett. 29, 1555 (1972), and private communication.
2. R. A. Laff and G. L. Hutchins, IEEE Trans. Electron Devices ED-21, 743 (1974).
3. W. C. Dash and R. Newman, Phys. Rev. 99, 1151 (1955).
4. G. G. MacFarlane, Phys. Rev. 111, 1245 (1958).
5. Solid State Research Report, Lincoln Laboratory, M.I.T. (1974:2), p.20, DDC AD-783634/9.
6. R. W. Powers and S. P. Mitoff, J. Electrochem. Soc. 122, 226 (1975).
7. A. Fujishima and K. Honda, Nature 238, 37 (1972).
8. Solid State Research Report, Lincoln Laboratory, M.I.T. (1975:1), p. 38, DDC AD-A009848.
9. M. Cardona and G. Harbeke, Phys. Rev. 137, A1467 (1965); W. J. Seouler and P. M. Raccach, Bull. Am. Phys. Soc. 15, 289 (1970); S. H. Shin, F. H. Pollak, T. Halpern, and P. M. Raccach, Solid State Commun. 16, 687 (1975).
10. P. B. Johnson and R. W. Christy, Phys. Rev. B 9, 5056 (1974).
11. J. C. C. Fan, Technical Report No. HP-28, Division of Engineering and Applied Physics, Harvard University (1972).
12. K. D. Sevier, Low Energy Electron Spectrometry (Wiley, New York, 1972), Chap. 8; Phys. Rev. 106, 874 (1957).
13. J. Colby, Seventh National Conference on Electron Probe Analysis, San Francisco, July 1972.

IV. MICROELECTRONICS

A. CHARGE-COUPLED IMAGING ARRAYS

Measurements of dark current have been made on the charge-coupled devices (CCDs) described in the two preceding reports.¹ These devices consist of a 100×1 linear CCD array and a 30×30 two-dimensional CCD array, which are being used as test vehicles working toward the long-range goal of a large-area imaging device for the TDAR Program. A low dark current will be essential for the operation of the final device.

Measured values of dark current in devices fabricated to date have been consistently greater than 500 nA/cm^2 at room temperature. By operating the CCD as a gated diode, it has been found that most of this generation current comes from the bulk material, and that the contribution from interface states is negligible in comparison. The corresponding bulk lifetimes are less than 1×10^{-6} sec, and appear to be less than those of the starting material used for these devices. Reported values² of dark current in CCDs are a factor-of-10 lower than the 500 nA/cm^2 we have measured, and for this reason we have begun experiments aimed at improving this aspect of the devices.

The principal source of bulk lifetime degradation in silicon is attributed to metallic contaminants such as Au, Cu, and Fe which introduce levels in the middle of the forbidden gap. Phosphorous gettering has been used for many years as a means of removing these contaminants. Such a gettering is included in our CCD fabrication during the diode diffusions (30 minutes, 1000°C) and doping of the polysilicon gates (20 minutes, 950°C), but it is apparent that additional gettering is necessary. A newer method of gettering which is gaining wide acceptance is the addition of small quantities of HCl during oxidation in dry O_2 (see Ref. 3). Our results have shown that a dramatic improvement in lifetime occurs with HCl, and we have obtained bulk lifetimes as high as 2.3 msec, which is comparable to the highest values yet reported.⁴

A simple and convenient method of measuring bulk and surface lifetimes is to pulse an MOS capacitor from accumulation to deep depletion, and monitor the capacitance as the device relaxes to the equilibrium condition of inversion. The experiments used p-type, (100)-oriented wafers from each of three vendors, and the resistivities, dislocation counts, and lifetime results for each material are listed in Table IV-1. Dislocation counts were made after 20 minutes in a

TABLE IV-1
RESULTS OF MEASUREMENTS ON Si WAFERS FROM THREE SOURCES
COMPARING BULK LIFETIME τ FOR OXIDATION IN PURE O_2 AND IN $\text{O}_2 + 5\% \text{ HCl}$

Material	Resistivity ($\Omega\text{-cm}$)	Dislocation Count (cm^{-2})	τ (O_2) (μsec)	τ ($\text{O}_2 + 5\% \text{ HCl}$) (μsec)
A	30	7,000	13 to 250	1200 to 2300
B	90	2,800	<3 to 180	700 to 1600
C	300	>10,000	<7	400 to 2200

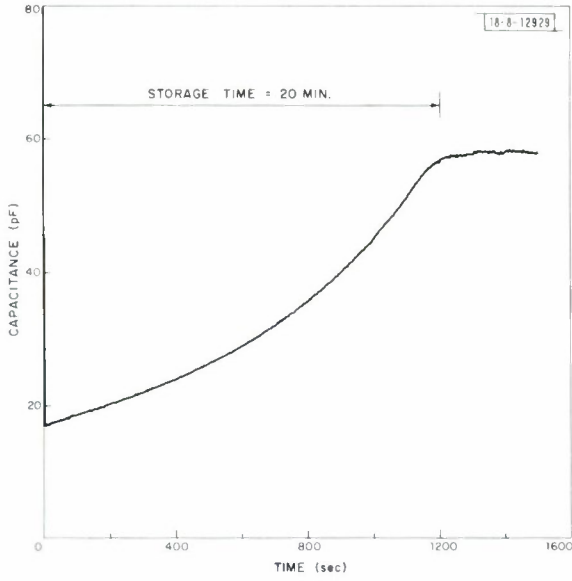


Fig. IV-1. Plot of capacitance vs time of MOS capacitor on material A (see Table IV-1). Capacitor is pulsed from -3 to +10 V at time 0 and allowed to relax to inversion. Storage time of 20 minutes was obtained in this case.

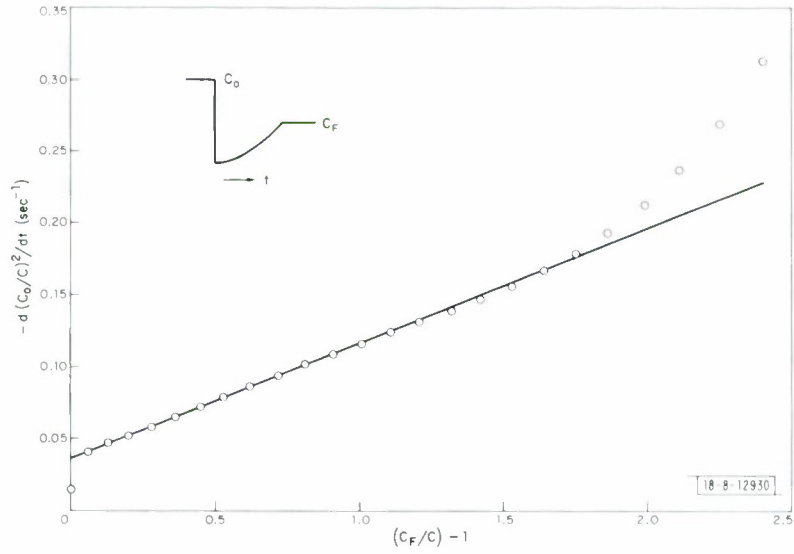


Fig. IV-2. Zerst plot of data of Fig. IV-1. A plot of $-d(C_O/C)^2/dt$ vs $(C_F/C) - 1$ yields a straight line portion whose slope is inversely proportional to bulk generation lifetime, which in this case is 2.3 msec.

Secco etch.⁵ In the first experiment, a 1200-Å oxide was grown in O₂ at 1100°C for 60 minutes, followed by a 30-minute anneal in N₂. Aluminum was filament-evaporated on the front and back (oxide removed) and the wafers were annealed at 500°C in N₂ for 15 minutes. MOS capacitors were patterned in the aluminum and consisted of circular dots of 1.09-mm diameter surrounded by a metal guard ring which was biased to suppress surface inversion. The results in Table IV-1 show wide variation in the lifetime in materials A and B, and a uniformly poor lifetime in material C. Measurements were performed on approximately ten capacitors on each wafer.

In the second experiment, the oxidation was performed in the presence of 5% HCl, and the dramatic improvement in lifetime can be seen in Table IV-1. An example of a pulsed C-t curve on material A is shown in Fig. IV-1. The capacitor was pulsed from strong accumulation (-3 V) to deep depletion (+10 V) at time 0, and capacitance was recorded as a function of time as it relaxed to the equilibrium value of C_F = 58 pF. The "storage time" in this case was 20 minutes. The Zerbst plot^{6,7} of these data is shown in Fig. IV-2. From an analysis of the linear portion of the curve, a bulk lifetime of 2.3 msec is obtained. The initial deviation of the curve from linear is used to derive the surface recombination velocity $s(t = 0) = s_0 = 0.15$ cm/sec. The exceptionally small value of s_0 corresponds to interface state densities of roughly 10^9 cm⁻² eV⁻¹ and are known to result from the presence of aluminum on the oxide during the 500°C anneal.

Unfortunately, it has been the experience of others that the lifetime degrades as a result of the many processing steps required in fabricating CCDs. For this reason, one must study the effects of these additional processing steps on the dark current. Such experiments are now under way.

B. E. Burke
R. A. Cohen
R. W. Mountain

B. TAPPED DELAY LINE

Work is continuing on a surface-acoustic-wave tapped delay line for the Re-entry Systems Program. The basic transducer design for this delay line was discussed in the preceding report.⁸ Further work on this design and preliminary experimental results on the delay line delivered to the R.F. Systems Group (Fig. IV-3) are reported here. The specifications for each crystal (corresponding to half the total delay) of the two-crystal delay line are listed in Table IV-2.

1.5-dB bandwidth	100 MHz
Center frequency	300 MHz
Maximum delay	33 μsec
Number of outputs	6
Matching between taps	±2 dB maximum
Spurious responses	-20 dB maximum

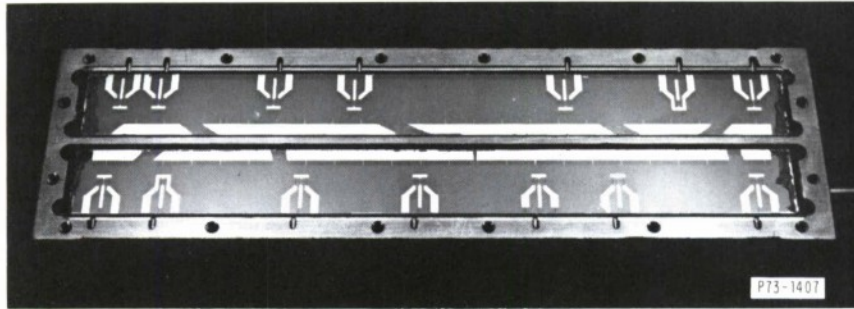


Fig. IV-3. Tapped-delay line with both LiNbO_3 crystals mounted and wire-bonded. Device is complete except for mounting package cover.

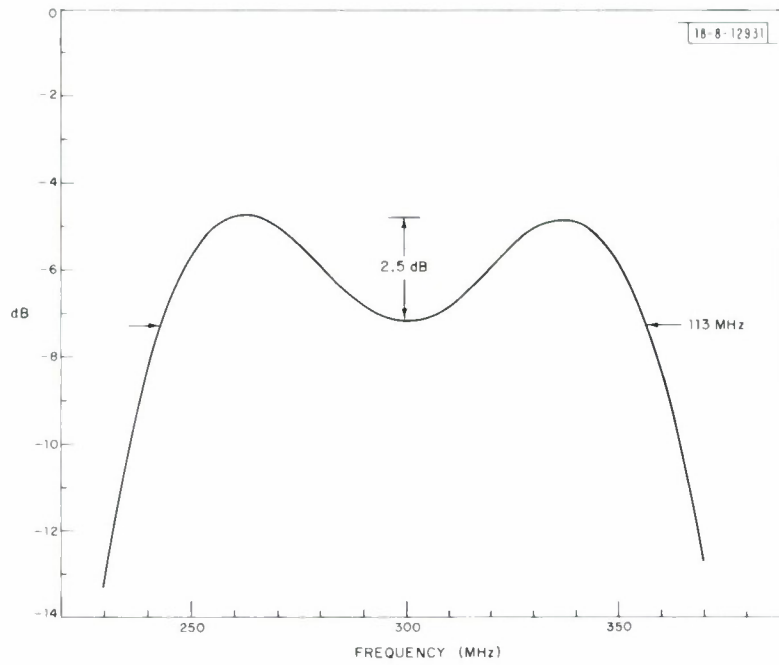


Fig. IV-4. Example of theoretical frequency response of output transducer for selected value of design centerline frequency of transducer. This curve is for centerline frequency of 300 MHz, with input a double-humped signal from a phase-reversal transducer.

In order to attempt to compensate for a propagation loss of 4 dB between the first and last output tap, the aperture of each output transducer (except the last) was reduced by an amount sufficient to increase its insertion loss so that all taps would have equal output at the center frequency.

Because the propagation loss of the double-humped signal launched by the phase-reversal input transducer increases with increasing frequency, the signal from each of the output transducers is skewed downward with frequency. To compensate for this distortion of the signals from the single-peak output transducers, the design centerline frequency of each of the output transducers was shifted upward in frequency from the nominal value of 300 MHz. The theoretical frequency responses⁹ of the transducers and the propagation loss were calculated for various values of the center frequency of the output transducer, and the overall theoretical frequency response was plotted (see Fig. IV-4) until an optimum was found for each tap. The center frequencies for each of the 5-finger output transducers are shown in Table IV-3.

Time Delay (μ sec)	Center Frequency (MHz)
Between 0 and 4	300
Between 9 and 21	308
Between 22 and 33	318

Two different 33- μ sec delay lines on 5.0- \times 0.5- \times 0.1-inch-thick LiNbO₃ crystals, each with six output taps at specified locations and incorporating the transducers discussed in the previous paragraphs, have been fabricated by the conformable mask and metal-lift technique. The transducer patterns for each delay line were replicated from three separate 2-inch-square masks, so a technique was needed for properly aligning the three masks and orienting them to the crystal axis. A special 2- \times 6-inch alignment mask was prepared and carefully aligned to the edge of each crystal which had been coated with chrome and photoresist. After exposure, development, and etching, the crystal had a series of standardized chrome alignment marks which were then matched to corresponding alignment marks on the 2- \times 2-inch transducer masks as each transducer mask was used.

The packaging of these delay lines presented some unusual problems. The package had to be lightweight, and yet sturdy enough to protect the fragile LiNbO₃ crystals. The space available on the circuit board determined that the width be held to a minimum. The package had to be pluggable and be compatible with its intended space environment. Excellent insulation between transducer taps, good electrical conductivity from the delay line to the package, and electromagnetic shielding between the two half-delay-lines were also required. The attachment method had to maintain adhesion and yet permit differential expansion between the crystal and the package.

These design requirements were met by fabricating two approximately 5.08- × 0.55- × 0.18-inch-deep cavities in a 5.45- × 1.54- × 0.36-inch-thick aluminum block (see Fig. IV-3). The aluminum then was anodized to provide insulation where required.

Gold-plated pins were mounted inside orifices in the package with a drop of RTV rubber to seal the hole and permit the application of an insulating epoxy from the reverse side.

The two half-delay-lines were installed in the separate cavities as described below. A layer of conductive, silver-filled, silicone rubber adhesive was applied to the bottom surfaces of the cavities which had been masked during anodizing to provide a clean metallic surface. A flexible pad of conductive elastomer was placed onto this layer of adhesive, and another layer of adhesive was "battered" onto the top of the pad. The LiNbO₃ crystal then was placed in the cavity to complete the mounting operation. The transducers were connected to the gold-plated input-output leads using an ultrasonic tailless bonder and 1-mil aluminum wire. The cover was mounted with a gold wire gasket to improve the seal.

Electrical tests on these delay lines showed that they have acceptable response. There was, however, one unexpected result. The output at the last tap was about 4 dB less than at the first, and the output decreased with distance along the lines. This result is in spite of the fact that the apertures of the output transducers were weighted to compensate for propagation loss. Nevertheless, all taps are within the ±2-dB specification.

The frequency response of all taps is identical, indicating that the compensation for the frequency dependence of the propagation loss was done correctly. It was noted in the previous report⁸ that the theoretical calculations underestimated the magnitude of the dip in the frequency response. These new results confirm this error, but show that the theory still is useful for determining the center frequency of the output transducer.

Although these delay lines have acceptable performance, work is continuing in an effort to reduce the size of the midband dip. Measurements made on a short experimental delay line, with the input transducer tuned with a series inductor and with one 5-finger and one 6-finger output transducer, yielded the results shown in Table IV-4.

Input	Output	Dip (dB)	Bandwidth (MHz)
Untuned	5-finger	3.5	130
Untuned	6-finger	2.6	113
Tuned	5-finger	1.9	114
Tuned	6-finger	1.4	100

A 12-finger phase-reversal input transducer also reduced the dip, but reduced the bandwidth to less than the 100-MHz specification. The reflection coefficient of the 6-finger output transducer was measured to be -22 dB - not significantly greater than for the 5-finger transducer.

D. L. Smythe T. F. Clough
F. J. Bachner L. L. Grant

C. SILICON SCHOTTKY-DIODE ARRAYS FOR COHERENT INTEGRATION OF ACOUSTIC SIGNALS

An acoustic correlator with a memory was reported in the previous Solid State Research Report (see p. 57 in Ref. 8). This device consists of a matrix of free-standing Schottky diodes on a silicon strip mounted in close proximity with a LiNbO_3 surface-wave delay line. The phase and amplitude of a signal launched into the delay line are recorded as a spatially varying charge pattern on the diode matrix by applying a voltage pulse across the composite Si- LiNbO_3 structure for a fraction of an RF cycle. The voltage pulse will transfer a uniform charge to the diodes, which back-biases them slightly after the pulse is turned off. The charge pattern can be stored in the diodes for a time determined by the leakage current through the back-biased diodes and the diode capacity. To increase the capacity of the diodes and thereby increase the storage time, each diode is overlaid by a surface island larger in area than the Schottky contact, as shown in Fig. IV-5.



Fig. IV-5. Silicon Schottky-diode array with polyerystalline silicon contacts. $10 \times 10\text{-}\mu\text{m}$ polysilicon areas appear as light gray squares which are overlaid on $5\text{-}\mu\text{m}$ Pt contact circles.

Experiments show that the charge stored in the array can be erased by the application of a second short-voltage pulse. Thus, the device is not able to record a succession of RF signals since the application of a new voltage pulse would erase the charge previously stored on the diodes.

We have modified the original configuration to provide for an accumulative overlay of signals written into the matrix in time succession. When the voltage pulse is exactly timed with respect to the RF signal, the charge from the same signal waveform can be added coherently by repetitive writing-in sequences. Since the stored-signal increase is proportional to the number of writing-in sequences N , and since the noise is expected to increase as $N^{1/2}$, the gain in signal to noise is $N^{1/2}$.

The modification of the original device to provide for this function is to replace the metal overlay islands by highly resistive polycrystalline silicon film islands. Most of the charge brought to the Schottky contacts by the writing-in pulse is accumulated in the polysilicon, since the capacitance between it and the bulk silicon is substantially larger than the junction capacitance of the Schottky contacts with zero or small reverse bias across the diodes. Since the relaxation time for the charge in the polysilicon is of the order of microseconds, subsequent voltage pulses will add charge to the diodes without erasing the charge already stored there. The experiments so far have shown a coherent integration gain of 20 dB over what is achieved with a single pulse. The gain presently is limited by the repetition rate of the equipment supplying the voltage pulse.

The fabrication procedure for the acoustic correlator described in the earlier report (Ref. 8, p. 57) was modified to include the deposition and etching of a high-resistivity polycrystalline film. 1200 Å of undoped high-resistivity (10^6 -ohm-cm) polycrystalline silicon was deposited in a vertical Ecco epitaxial reactor from SiH_4/Ar in N_2 ambient at 650°C. The contact pads were delineated by conventional photolithography and the silicon was etched in a cold (7°C) mixture of 50 $\text{HNO}_3/1$ $\text{HF}/1$ HAC to form 10×10 - μm pads on 12.6- μm centers overlaying the 5- μm Pt-Si Schottky barrier diodes. The 800- \times 100-mil strips were separated by a 2-mil diamond saw blade followed by a brief isotropic etch in 50 $\text{HNO}_3/1$ $\text{HF}/1$ HAC to remove saw damage and present a smooth surface to acoustic waves.

K. Ingebrigtsen
R. A. Cohen
R. W. Mountain

D. GALLIUM ARSENIDE VAPOR EPITAXY

Many of the microwave and integrated optical devices being developed at Lincoln Laboratory require multiple semiconductor layers of differing doping levels and differing doping materials on highly doped substrates. To meet some of these material requirements, a new system for vapor epitaxy of GaAs has been constructed. The major objectives in the design of this system were to have the most accurate control possible, and to have versatility without sacrificing crystal quality. In addition, it has been realized that the system will go through considerable evolution to meet changing materials requirements.

The most commonly used vapor-phase technique for the epitaxial growth of GaAs is the AsCl_3 -Ga- H_2 method.¹⁰⁻¹² Because of its high state of development, this method was chosen for our system, a schematic of which is given in Fig. IV-6. One unusual feature of the system is a vertical furnace in contrast to the more commonly used horizontal furnace. The vertical arrangement allows the furnace reactor tube to be opened at the bottom to load and unload substrates without losing the hydrogen atmosphere inside the tube. Thus, the furnace can remain at growth temperatures while loading and unloading, which decreases the cycle time between runs. Another advantage of the vertical furnace is that it allows pedestal rotation, which is expected to result in greater epitaxial layer uniformity.

The temperature profile of the furnace (see Fig. IV-6) is arranged to provide a Ga source temperature of 820°C, a substrate etch temperature of 790°C, a layer growth temperature of 740°C, and a preheat temperature of 780°C. When the reactor tube is opened for loading, there is a purge flow of hydrogen passing down the inside of the backflow tube. The hydrogen flows out into a nitrogen box which surrounds the opening. After the tube is closed, the flow reverses

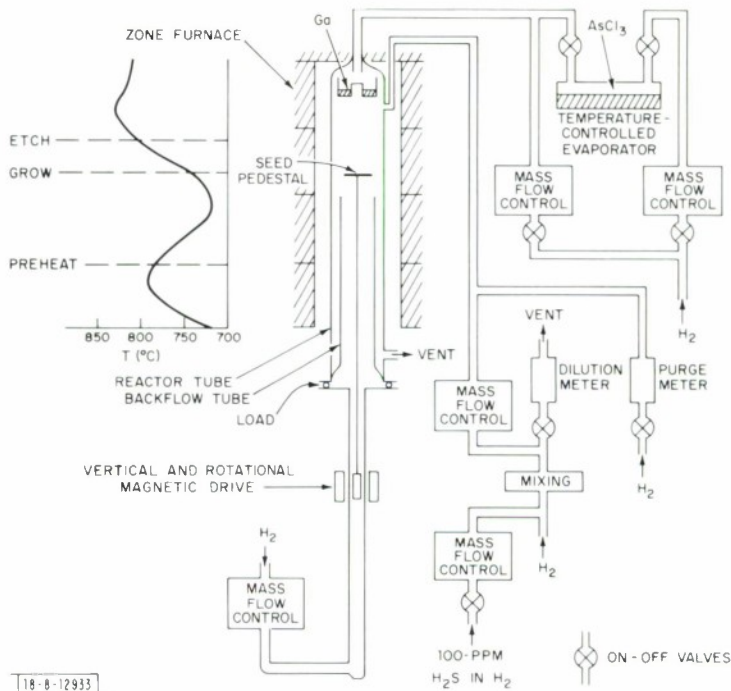


Fig. IV-6. Schematic of GaAs vapor-epitaxy system.

and is up the inside of the backflow tube and down between the backflow tube and the reactor tube. The reverse flow is maintained while the substrate is moved from the load position up into the furnace to the preheat position. At the same time, the proper growth conditions can be established in the upper part of the furnace by turning on the AsCl_3 and dopant flows. The reverse flow of hydrogen is sufficient to stop the back diffusion of reactants into the preheat position. When the substrate has reached proper temperature, it then can be moved into either the etch or growth position. The substrate can be returned to the pure hydrogen environment while establishing a new dopant level, and subsequently returned to the growth position for any number of succeeding layers. The flow rate used for layer growth is in the range 500 to 800 cc/min. using a 60-mm ID reactor tube. The dopant gas is hydrogen sulfide, and the concentration is controllable over a wide range with a dilution system.

The epitaxy system has produced very reproducible uniform layers with excellent surface smoothness. Some layers have no visible surface features using interference contrast microscopy with magnifications up to 1300X. Sulfur-doped layers have been grown at doping levels from $5 \times 10^{14} \text{ cm}^{-3}$ to $3 \times 10^{18} \text{ cm}^{-3}$ on substrates which were silicon-doped at a level of 10^{18} cm^{-3} . Hall measurements (van der Pauw method) were made on layers grown on chromium-doped substrates. These layers were grown simultaneously with the layers on highly doped substrates. The liquid nitrogen mobilities have ranged up to $80,000 \text{ cm}^2/\text{V sec}$, which implies¹³ a total impurity level, $N_A + N_D$, of $1 \times 10^{15} \text{ cm}^{-3}$. The present effort is directed toward growth of specific layers for IMPATT diodes, FETs, and optical waveguides.

C. O. Bozler

REFERENCES

1. Solid State Research Reports, Lincoln Laboratory, M.I.T. (1974:4), p. 57, DDC AD-A004763/9, and (1975:1), p. 56, DDC AD-A009848.
2. C. H. Sequin, F. J. Morris, T. A. Shankoff, M. F. Tompsett, and E. J. Zimavy, Jr., IEEE Trans. Electron Devices ED-21, 712 (1974).
3. P. H. Robinson and F. P. Heiman, J. Electrochem. Soc. 118, 141 (1971).
4. S. Nishimatsu, T. Iwasaki, and M. Ashikawa, Abstract No. 147, Electrochemical Society Meeting, May 1975.
5. F. Secco d'Aragona, J. Electrochem. Soc. 119, 948 (1972).
6. M. Zerbst, Z. Angew. Phys. 22, 30 (1966).
7. D. K. Schroder and H. C. Nathanson, Solid-State Electron. 13, 577 (1970).
8. Solid State Research Report, Lincoln Laboratory, M.I.T. (1975:1), p. 58, DDC AD-A009848.
9. T. W. Bristol, "Synthesis of Periodic Unapodized Surface Wave Transducers," 1972 Ultrasonics Symposium Proceedings, October 1972.
10. C. M. Wolfe, A. G. Foyt, and W. T. Lindley, Electrochem. Technol. 6, 208 (1968), DDC AD-673592.
11. J. V. DiLorenzo, J. Cryst. Growth 17, 189 (1972).
12. D. W. Shaw, J. Cryst. Growth 8, 117 (1971).
13. C. M. Wolfe, G. E. Stillman, and J. O. Dimmock, J. Appl. Phys. 41, 504 (1970), DDC AD-707572.

REPORT DOCUMENTATION PAGE		READ INSTRUCTIONS BEFORE COMPLETING FORM
1. REPORT NUMBER ESD-TR-75-170	2. GOVT ACCESSION NO.	3. RECIPIENT'S CATALOG NUMBER
4. TITLE (and Subtitle) Solid State Research		5. TYPE OF REPORT & PERIOD COVERED Quarterly Technical Summary, 1 February - 30 April 1975
		6. PERFORMING ORG. REPORT NUMBER 1975:2
7. AUTHOR(s) McWhorter, Alan L.		8. CONTRACT OR GRANT NUMBER(s) F19628-73-C-0002
9. PERFORMING ORGANIZATION NAME AND ADDRESS Lincoln Laboratory, M. I. T. P. O. Box 73 Lexington, MA 02173		10. PROGRAM ELEMENT, PROJECT, TASK AREA & WORK UNIT NUMBERS Project No. 649L
11. CONTROLLING OFFICE NAME AND ADDRESS Air Force Systems Command Andrews AFB Washington, DC 20331		12. REPORT DATE 15 May 1975
		13. NUMBER OF PAGES 68
14. MONITORING AGENCY NAME & ADDRESS (if different from Controlling Office) Electronic Systems Division Hanscom AFB Bedford, MA 01731		15. SECURITY CLASS. (of this report) Unclassified
		15a. DECLASSIFICATION DOWNGRADING SCHEDULE
16. DISTRIBUTION STATEMENT (of this Report) Approved for public release; distribution unlimited.		
17. DISTRIBUTION STATEMENT (of the abstract entered in Block 20, if different from Report)		
18. SUPPLEMENTARY NOTES None		
19. KEY WORDS (Continue on reverse side if necessary and identify by block number)		
solid state devices	photodiode devices	imaging arrays
quantum electronics	lasers	surface wave transducers
materials research	laser spectroscopy	EAP detectors
microelectronics	infrared imaging	
20. ABSTRACT (Continue on reverse side if necessary and identify by block number)		
<p>This report covers in detail the solid state research work of the Solid State Division at Lincoln Laboratory for the period 1 February through 30 April 1975. The topics covered are Solid State Device Research, Quantum Electronics, Materials Research, and Microelectronics. The Microsound work is sponsored by ABMDA and is reported under that program.</p>		